CHALMERS

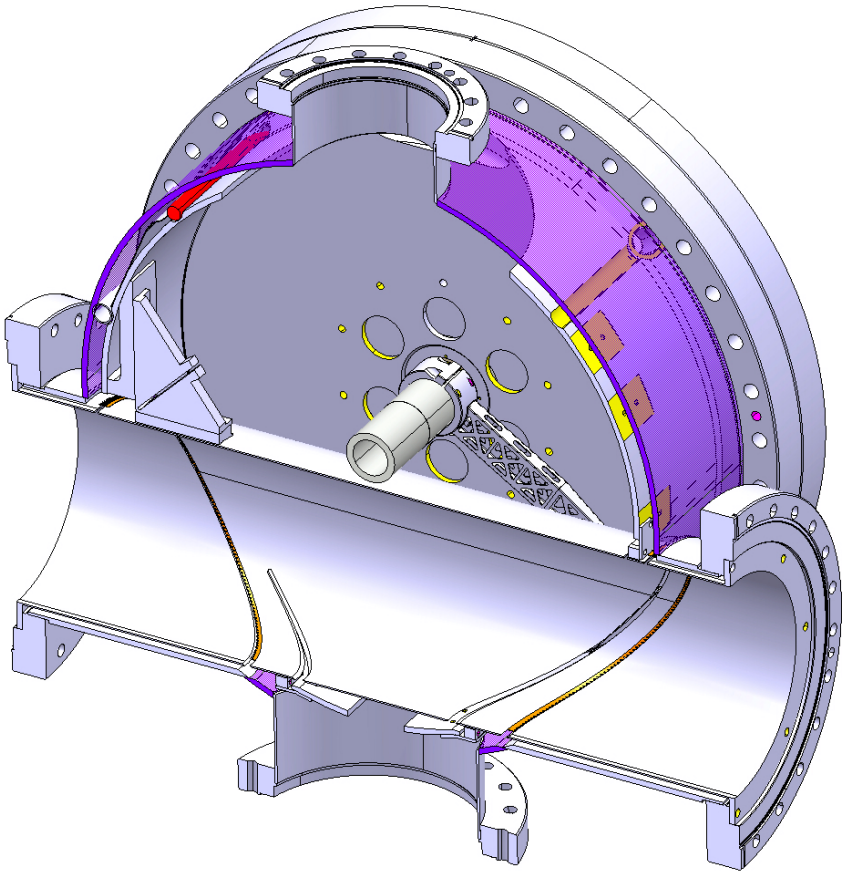

Mechanical optimisation of a high-precision fast wire scanner at CERN

Master's thesis in the master's programme Applied Mechanics

SEBASTIAN SAMUELSSON

Department of Applied Mechanics
Division of Dynamics
CHALMERS UNIVERSITY OF TECHNOLOGY
Gothenburg, Sweden 2013
Master's thesis 2013:22

MASTER'S THESIS IN THE MASTER'S PROGRAMME APPLIED MECHANICS

Mechanical optimisation of a high-precision fast wire scanner at CERN

SEBASTIAN SAMUELSSON

Department of Applied Mechanics
Division of Dynamics
CHALMERS UNIVERSITY OF TECHNOLOGY
Gothenburg, Sweden 2013

Mechanical optimisation of a high-precision fast wire scanner at CERN
SEBASTIAN SAMUELSSON

Master's thesis 2013:22
ISSN 1652-8557
Department of Applied Mechanics
Division of Dynamics
Chalmers University of Technology
SE-412 96 Gothenburg
Sweden
Telephone: +46 (0)31-772 1000

Cover:
The figure shows a section of the wire scanner assembly. A cut through the length of the RF screen (the grey pipe) and the slots which allow wire passage are shown as well as the surrounding vacuum tank (purple). The shaft and fork visible in the model have been designed and optimised as a part of the present thesis.

Chalmers Reproservice
Gothenburg, Sweden 2013

Mechanical optimisation of a high-precision fast wire scanner at CERN
Master's thesis in the master's programme Applied Mechanics
SEBASTIAN SAMUELSSON
Department of Applied Mechanics
Division of Dynamics
Chalmers University of Technology

Abstract

Wire scanners are instruments used to measure the transverse beam profile in particle accelerators by passing a thin wire through the particle beam. To avoid the issues of vacuum leakage through the bellows and wire failure related to current designs of wire scanners, a new concept for a wire scanner has been developed at CERN. This design has all moving parts inside the beam vacuum and has a nominal wire scanning speed of 20 m/s. The demands on the design associated with this together with the high precision requirements create a need for careful optimisation of the mechanical components in the wire scanner assembly. In the present thesis, a thin vacuum wall (0.3 mm thick), which fits in the air gap (approximately 0.8 mm) between the rotor and the stator of the electric motor has been designed to separate the moving in-vacuum parts from the stationary components under ambient conditions. Furthermore, the material of the shaft has been selected as 316L stainless steel to best comply with the operational conditions. The shaft of the wire scanner has also been dimensioned to minimise the shaft twist and hence the misalignment between the forks holding the wire. Further, as a part of this thesis, the wire scanner forks have been topologically optimised in order to ensure a low inertia and low vibrational amplitude. Based on this optimisation, a CAD-model of the fork has been developed, which will be manufactured in titanium using metal additive manufacturing (3D-printing). A plastic prototype of the fork has been successfully manufactured using such a manufacturing method. Finite element simulations carried out in ANSYS verify that the precision requirement of 5 µm in uncertainty of the fork tip position is met using a sinusoidal acceleration profile similar to the acceleration foreseen for the new wire scanner. Based on the outcomes of the present thesis, the components will be manufactured during the summer of 2013 and used in the first prototype of the new fast wire scanner. Another prototype is planned to be installed in the Super Proton Synchrotron (SPS) at CERN during 2014. The intention is then that the final design of the new fast wire scanner should be installed in all accelerators at CERN during the second long shutdown (LS2) in 2018-2019.

Keywords: CERN, Particle accelerators, Wire scanner, Beam instrumentation, Transverse profile measurements, Topology optimisation, Ultra-high vacuum, Metal additive manufacturing, 3D-printing

Acknowledgements

I would like to thank all the members of the wire scanner project group. Especially I would like to thank my supervisor, Raymond Veness, and Juan Herranz Alvarez for their valuable input and support during my stay at CERN. Thank you also to all of my colleagues in the Mechanics and Logistics Section as well as the Beam Loss Section of the Beam Instrumentation Group at CERN, for making the duration of this thesis a memorable year. Finally, I would like to extend my thanks to my examiner at Chalmers University of Technology, Mikael Enelund, for his guidance and supervision.

Contents

1 Introduction

This master's thesis is conducted at the European Organization for Nuclear Research (CERN), which is a particle physics laboratory that uses particle accelerators to study the fundamental consistuents of matter. In order for these accelerators to function properly, carefully designed instrumentation is of fundamental importance. In this thesis, several mechanical components of one of these instruments, a fast wire scanner, are optimised. In this chapter an introduction to CERN and particle accelerators as well as the background and objectives of the present thesis are given.

1.1 CERN

CERN is one of the world's largest scientific research centres. It was founded in 1954 and it is situated on the border between France and Switzerland near Geneva. It was one of Europe's first joint ventures and currently has 20 member states. CERN employs almost 2400 people. In addition to this, approximately 10000 visiting scientists, who correspond to half of the world's particle physicists, come to CERN for their research [1]. The organisation has four main missions. The most publicly known of these missions is to conduct fundamental physics research. A further mission of CERN is to share the technologies developed for its research in order for it to be used in other applications. CERN's third mission is to educate the communities of its member states in the field of science and CERN also serves to create a collaborative environment between its member states, which is its fourth mission.

1.1.1 Research at CERN

The main research focus at CERN is particle physics, the study of the fundamental constituents of matter. Since the 1970s, the standard model has been used to describe everything that can be observed in the universe [2]. The standard model stipulates that the visible universe is made of a number of building blocks called fundamental particles, held together by four fundamental forces. However, according to our understanding, the standard model only describes 4% of the known universe [2]. The rest is postulated to be made up of dark matter and dark energy. Using powerful particle accelerators, the experiments at CERN aim to study these things. Other goals are to understand the Higgs boson, that gives other particles mass, and to investigate if there is evidence for a theory called supersymmetry [2].

The Standard Model

The Standard Model collects the current knowledge of fundamental particles and forces. It says that leptons and quarks are the fundamental building blocks of matter. There are six leptons (the electron, electron neutrino, muon, muon neutrino, tau and the tau neutrino) as well as six quarks (up, down, charm, strange, top and bottom quarks) [2]. These are held together by four fundamental forces, which are each carried by a so called carrier particle.

The quarks are held together and combine into protons and neutrons by the strong force, which is carried by a particle known as the gluon [2]. It also holds protons and neutrons together in atomic nuclei. It is referred to as strong because it overcomes the repulsive force occuring in nuclei due to the positive charge of the protons. The second fundamental force is the electromagnetic force whose carrier particle is the photon [2]. It is felt by the quarks and charged leptons and is responsible for holding electrons to nuclei, and for binding atoms together into molecules. The third fundamental force is the weak force which acts on both quarks and leptons. Its carrier particles are the intermediate vector bosons (W^-, W^+ and Z^0). It is the force behind natural radioactivity and is also responsible for nuclear fusion in stars like our Sun, where hydrogen atoms combine into helium. The fourth fundamental force is gravity, which is an attractive force and is relatively weak compared with the other fundamental forces [2].

The Higgs mechanism

The Standard Model has not been able to explain how particles obtain mass, and why some particles are more massive than others. According to the theory of the Higgs mechanism, the entire space is filled with a Higgs

field through which the fundamental particles gain their mass. The more a particle interacts with this field the more mass it acquires. The Higgs field has at least one new particle associated with it, the Higgs boson. During the course of 2012 and 2013 evidence for a particle consistent with a Standard Model Higgs boson was revealed by the ATLAS and CMS experiments at CERN [3, 4].

Supersymmetry

A unification of all fundamental forces in the Standard Model has not been achieved, due to the difficulty of incorporating gravity in a similar way to the other forces. Supersymmetry could be capable of unifying the fundamental forces. The supersymmetric theory suggests that there exist more massive partner particles of the known fundamental particles [2]. If the theory is correct, the lightest supersymmetric particles should be discovered in the experiments at CERN.

Dark matter and dark energy

Through cosmological and astrophysical observations it has been shown that visible matter accounts for merely 4% of the Universe. The rest is postulated to be made up of dark matter (23%) and dark energy (73%) [2]. A popular theory is that dark matter could be made up of supersymmetric particles (if they exist). The supposed existence of dark matter was found through astronomical observations and gravitational calculations which showed that there must be something more in the Universe than what can be observed by sight. These measurements also made it possible to estimate the quantity of what is assumed to be dark matter present in the Universe and its density, although it cannot be directly observed. It is now believed that the gravitational effect of dark matter makes galaxies spin faster than first expected and that its gravitational field deviates the light of objects behind it [2].

Dark energy is postulated to be evenly distributed through the entire Universe and throughout time [2]. This means that its effect is not diluted as the Universe expands. Its homogeneous distribution would also have the effect that it would not have any local gravitational effects but rather a composed global effect on the whole Universe. This would cause a repulsive force, tending to accelerate the expansion of the Universe. The rate of this expansion and its acceleration can be measured by experiments and have confirmed the presence of dark energy and provided an estimate of its amount [2].

Antimatter

The amount of matter and antimatter created in the Big Bang must have been the same, but from what has been observed so far our Universe consists only of matter [2]. This imbalance between matter and antimatter could possibly be explained by that matter and antimatter are not perfect reflections of each other. The strongest limits on the amount of antimatter in space come from the analysis of diffuse cosmic gamma-rays and the inhomogeneities in what is known as the cosmic microwave background (CMB) [2]. If the Universe somehow split into different domains containing either matter or antimatter (and given that matter and antimatter annihilate and create cosmic rays when they come in contact) cosmic rays should be produced at the boundaries of these domains. If things such as annihilation cross-sections and distance are taken into account, the amount of diffuse cosmic radiation arriving on Earth can be predicted. When this prediction is compared with the measured influx of gamma radiation any domain size below 3.7 giga light years can be excluded [2]. This number is not so far from the size of the entire Universe. Another limit can be derived by analysing the inhomogeneitites in the CMB. An antimatter domain would cause heating of the domain boundaries, which would show up as density fluctuations in the measurements [2].

1.2 Particle accelerators

Particle accelerators were invented to provide high-energy particles in order to investigate the structure of the atomic nucleus. They accelerate and consequently increase the energy of particle beams by generating electric fields that speed up the particles and magnetic fields that steer and focus them. Accelerators are built either in the shape of a ring (circular accelerators) or in a straight line (linear accelerators). The three main components in an accelerator are [1]:

- Radiofrequency (RF) cavities and electric fields which accelerate the particle beam by means of transferring the energy in the radio-wave to the particles.
- Vacuum pipes inside which the particle beam travels. The metal pipes are kept at ultra-high vacuum to ensure that a minimum amount of gas molecules are present hence avoiding collisions between the beam and the gas molecules.
- Magnets which fulfil different functions in the accelerator. Dipole magnets are used to bend the particle beam (in circular accelerators) and quadrupole magnets are used to focus the beam to increase the energy density.

Due to the radiofrequency waves, the particles will organise themselves as tiny packets, or bunches, with a certain spacing in between each other. These bunches together make up the particle beam. The beams are then made to collide either with each other (two beams head on) or with stationary targets, for example metal plates. The effects of these collisions are subsequently studied in different experiments using particle detectors [1]. In order to obtain higher energies of the particles a number of accelerators can be connected sequentially. The energy of the beam then increases successively with each accelerator. Such a serial connection of accelerators makes up CERN's accelerator complex.

1.2.1 The CERN accelerator complex

The CERN accelerator complex (see Fig. 1.2.1) is a sequence of particle accelerators that can reach increasingly higher energies [1]. The particle beam is boosted in each of the accelerators before it is injected via a transfer tunnel (TT) into the next accelerator in succession. The accelerator complex also includes the Antiproton Decelerator (AD) and the Isotope Separator On-Line Device (ISOLDE) and feeds the Compact Linear Collider Study (CLIC) test facility, CTF3 [1].

In the Large Hadron Collider (LHC) physics programme mainly two classes of particles are studied, protons and heavy ions (lead ions in this case). Protons are obtained from stripping the electrons off hydrogen atoms. The protons then start accelerating in the linear accelerator LINAC 2 before they are injected into the PS Booster at an energy of 50 MeV [2]. After being accelerated to 1.4 GeV in the Booster, the protons are fed to the Proton Synchrotron (PS) where they are accelerated to 25 GeV. They are then transferred to the Super Proton Synchrotron (SPS) where the beam is accelerated to 450 GeV before it reaches the LHC which is the highest energy accelerator at CERN. The protons circulate in the LHC for 20 minutes before reaching their maximum speed and energy [2].

The lead ions for the LHC are obtained from a purified lead sample heated to about 500°C. An electric current is then used to ionise the lead vapour, producing a number of charged states with a maximum around Pb^{29+} [2]. These ions are then picked out and accelerated to 4.2 MeV/u (energy per nucleon) in the LINAC 3. They are subsequently passed through a thin carbon foil in order to strip most of them to Pb^{54+} before entering the Low Energy Ion Ring (LEIR). The Pb^{54+} beam is then accumulated after which it is accelerated to 72 MeV/u in the LEIR before being sent to the PS. In the PS, the ions are accelerated to 5.9 GeV/u before being fully stripped to Pb^{82+} by a second foil [2]. The beam is then passed to the SPS which accelerates it to 177 GeV/u. After that, the lead ions are transferred to the LHC where they are accelerated to 2.76 TeV/u.

The accelerator complex is controlled from the CERN Control Centre (CCC) where also the cryogenic distribution system, used for cooling the magnets, and the rest of the technical infrastructure is controlled.

1.2.2 The Large Hadron Collider (LHC)

The LHC, operating since 2008, is the highest energy particle accelerator in the world. It consists of two rings approximately 27 km in circumference inside which two particle beams travel in opposite directions. They are accelerated to an energy of 4 TeV each and are made to collide with each other at four intersection points (giving a total collision energy of 8 TeV). Huge particle detectors have been constructed at these four points to study the products of the collisions. In February 2013 the LHC was stopped for its first long shutdown (LS1). During LS1 maintenance on the machine will be carried out so that the LHC, when restarted in 2015, can reach an energy of 7 TeV per proton beam (and 1150 TeV for heavy ions).

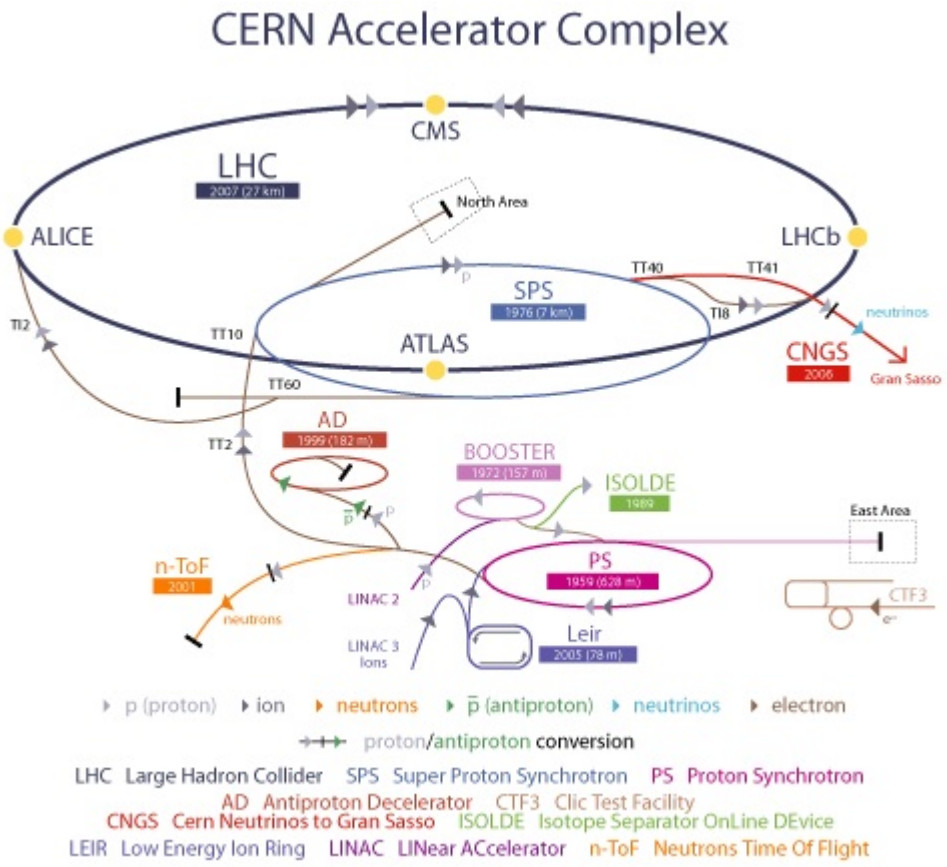

Figure 1.2.1: Overview of the CERN accelerator complex [1].

1.2.3 Accelerator parameters

Since the probability of the processes studied in the experiments at CERN vary with collision energy and because they are often rare, it is important to maximise the beam energy as well as the number of events (collisions). The number of events is expressed according to Eq. 1.2.1 [5].

$$N_{\text{event}} = L\sigma_{\text{event}} \tag{1.2.1}$$

where L denotes the luminosity and σ_{event} the cross-section for the studied event. The luminosity is a measure of the number of particle interactions (collisions) and it depends on the number of particles in each bunch, the number of bunches per beam, the frequency of complete turns around the accelerator and the cross-section of the beam. In order to maximise the luminosity, the particles need to be squeezed into a minimum amount of space around the beam interaction points. For the LHC, the luminosity is written [5]:

$$L = \frac{N_{\text{b}}^2 n_{\text{b}} f_{\text{rev}} \gamma_{\text{r}}}{4\pi\epsilon_{\text{n}}\beta^*} F \tag{1.2.2}$$

where N_{b} denotes the number of particles per bunch, n_{b} the number of bunches per beam, f_{rev} the revolution frequency, γ_{r} the relativistic gamma factor (related to the speed) and ϵ_{n} the normalised transverse beam emittance, while β^* is the beta function at the interaction point (proportional to beam amplitude) and F is the geometric luminosity reduction factor (which appears due to that the beams cross each other at an angle when they collide). The emittance is a measure of the average spread of particles in a beam. It is calculated from the beam width σ as [6]:

$$\epsilon = \frac{1}{\beta\left(s\right)}\left(\sigma^2 - \left(D\left(s\right)\frac{\Delta p}{p}\right)^2\right) \tag{1.2.3}$$

where $D(s)$ is the dispersion and $\beta(s)$ the beta function at the point of measurement (s). These can be measured separately. $\Delta p/p$ is the momentum spread of the particle beam [6]. The normalised emittance is then expressed as [5]:

$$\epsilon_{\text{n}} = \frac{v_{\text{s}}}{c}\gamma_r\epsilon \tag{1.2.4}$$

where v_{s} is the longitudinal beam velocity and c is the speed of light. The geometric luminosity factor is written [5]:

$$F = \left(1 + \left(\frac{\theta_{\text{c}}\sigma_{\text{z}}}{2\sigma^*}\right)^2\right)^{-1/2} \tag{1.2.5}$$

Here, θ_{c} is the full crossing angle at the point of collision, σ_{z} the root-mean-square (RMS) bunch length and σ^* the transverse RMS beam size at the interaction point. Together, these equations show the importance of being able to correctly measure the beam size. In order for this to function, well-designed beam instrumentation is of crucial importance.

1.2.4 Beam instrumentation and diagnostics

Beam instrumentation is a vital component of all particle accelerators. It allows to diagnose, *i.e.*, to show the behaviour and the properties of the particle beam. Without it, there would be no way to determine the settings of the accelerator or to make any improvements of these. Examples of properties that need to be known are beam current, beam profile and beam losses, amongst many others [6]. This project will be focused on an instrument used for beam profile measurements.

1.2.5 Beam profile measurements

The beam profile can be influenced by quadrupole magnets which are installed in all accelerators as well as in transfer lines between the accelerators. As Sec. 1.2.3 shows, it is of utmost importance to control the beam width, as well as matching the transverse profile of the beam between different parts of the accelerator. Since the number of bending, focussing and correction magnets in an accelerator is large many stations for profile measurements are needed. The measurement of the transverse beam profile is readily done by a wire scanner, which is a relatively non-destructive method for beam profile measurement [6].

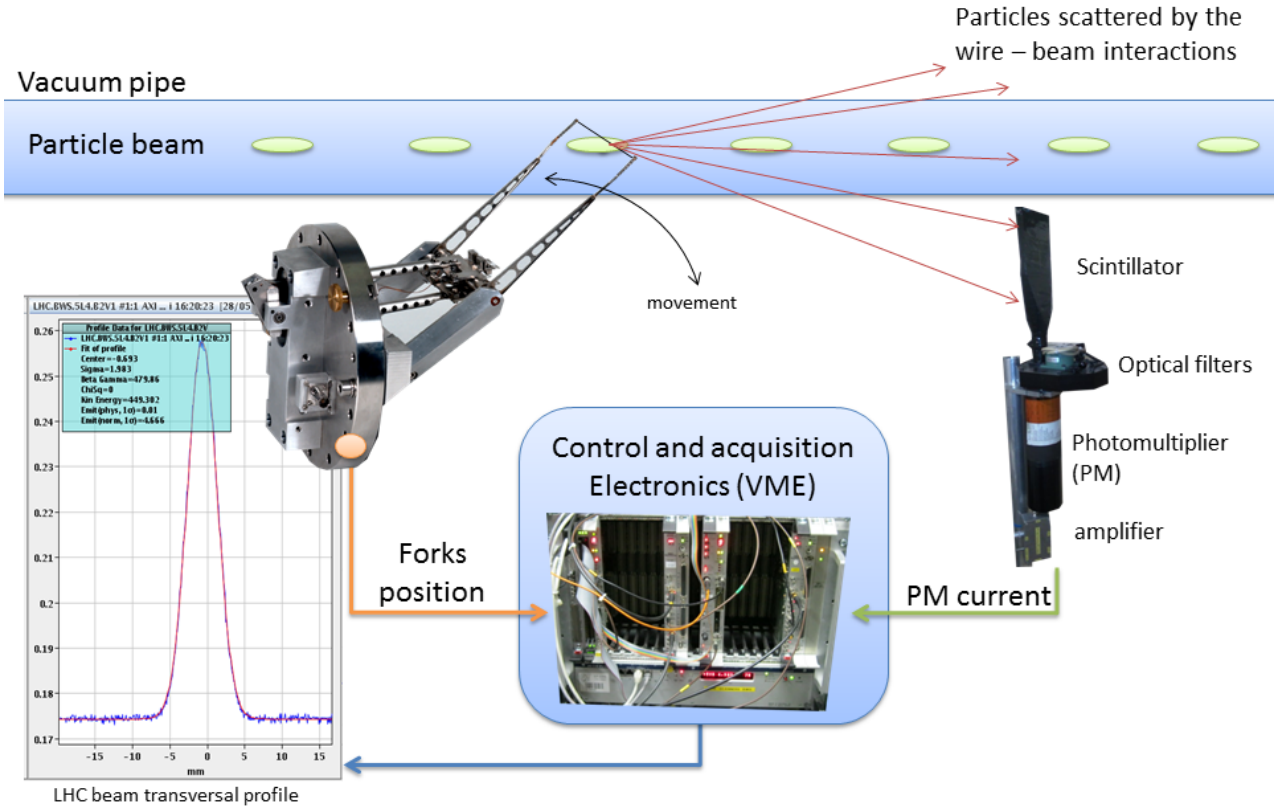

Figure 1.2.2: Schematic outline of the working principle of a rotary wire scanner [7]. The beam profile with the beam intensity (number of particles) on the vertical and the beam width on the horizontal axis is shown on the left.

1.2.6 Wire scanner

A wire scanner passes a thin wire through the particle beam (one out-scan and one in-scan) and this creates a shower of secondary particles. A scintillator measures the flux of particles scattered by the interaction of beam and wire. When this data is combined with the wire position during the course of the scan the transverse beam profile (*i.e.*, its distribution over the width) can be reconstructed. The working principle is shown schematically in Fig. 1.2.2. The wire material is chosen as carbon or silicon carbide (SiC) due to their low weight and low nuclear charge, which results in a low temperature increase of the wire [6]. Furthermore, these materials have a high melting temperature, also under vacuum conditions. The thickness of the wire can be as small as 10 microns. However, due to the single wire used in the scanner the instantaneous distribution cannot be obtained, even at high scanning velocities, and therefore only the steady-state profile can be probed [6]. Wire scanners are also frequently used in the accelerators at CERN to calibrate other profile measurement instruments in operation.

1.2.7 Present design of rotary wire scanners at CERN

The wire scanner consists of a motor which is mounted outside the vacuum pipe, *i.e.*, in atmospheric conditions. The mechanical motion is then transmitted through bellows to the fork of the scanner which is in vacuum. There are however some problems associated with this design. Firstly, for high intensity beams, the wire can fail due to the energy deposited in it [8]. Also the energy transferred to the wire from the beam's accompanying electromagnetic field can destroy the wire. Secondly, the position measurements of the wire have a level of inaccuracy due to the accuracy of the angular sensors as well as vibrations of the fork and wire which are induced by the fast acceleration (and deceleration) of the wire as well as the way the motor is controlled. The inaccuracies are further increased by the relatively complex mechanics that drive the shaft. Furthermore the bellows lose their sealing after a large amount of loading cycles due to fatigue failure. The actuator feedthrough

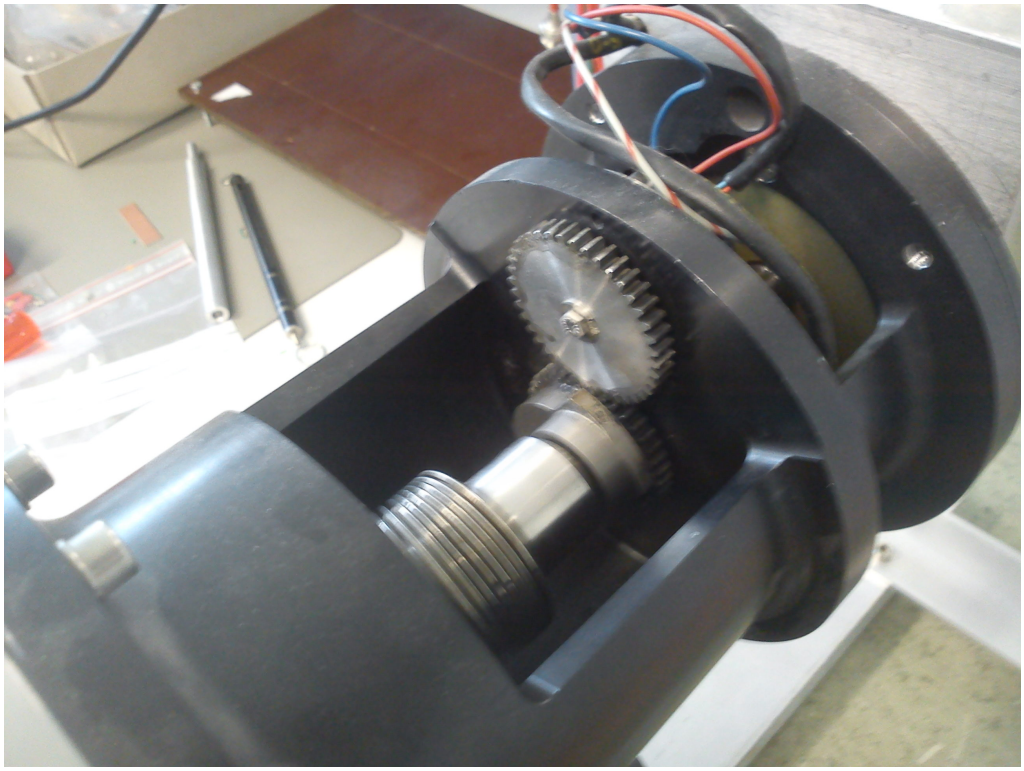

Figure 1.2.3: Actuator feedthrough of the rotary wire scanner used in the Super Proton Synchrotron (SPS) at CERN. To the left, the bellows are shown and to the right the gear transferring the motion from the motor shaft to the scanner shaft is visible.

of the rotary wire scanner type which is currently installed in the SPS at CERN is shown in Fig. 1.2.3.

1.3 Project background

To improve the design of fast wire scanners used at CERN, a new concept has been developed over the last few years [9]. The concept has been developed with a few main objectives. First of all, the problems with the current design, including vacuum leakage and wire failure need to be mitigated. Secondly, the precision of the measurements must be improved. Finally, it would be an advantage from a maintenance viewpoint to create one universal wire scanner design for use across all the accelerators at CERN, to replace the several different ones currently in use.

1.3.1 Conceptual design of a new fast wire scanner

In order to minimise the energy deposited in the wire and hence to avoid wire failure, the new fast wire scanner has been specified for a nominal wire scanning velocity (*i.e.*, the speed it has when it crosses the beam) of 20 m/s. The fatigue-prone bellows have been removed in the new concept and instead all the moving wire scanner components are mounted on one single shaft. This also has the advantage that it reduces the mechanical complexity of the instrument. This means that all rotating components are kept under vacuum and instead of using bellows to feed the mechanical movement into vacuum a thin wall separates the moving and stationary parts. The positions of the forks are measured by an optical encoder system, consisting of a glass disc with a chromed pattern held by a metal disc holder. The positions of the forks together with the position of the motor (which is obtained from the resolver) are combined to determine where the wire is during the scan. The new fast wire scanner concept is shown in Fig. 1.3.1.

During transport and installation, unplanned movements of the forks are not welcome. Also, in case of a power or control system failure during operation, the forks and wire could move in an uncontrolled fashion into the

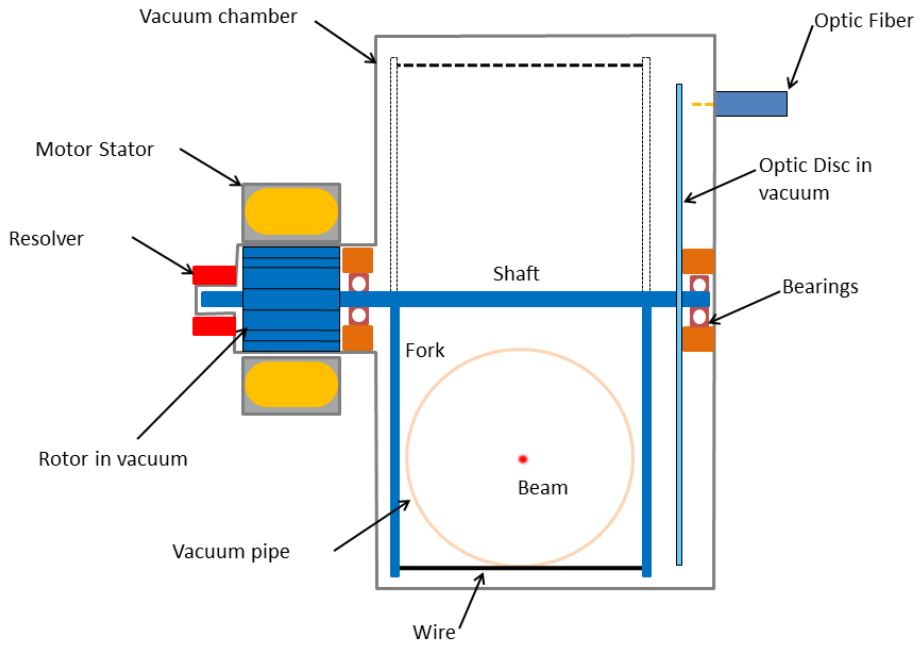

Figure 1.3.1: Schematic drawing of the new fast wire scanner concept.

beam aperture. This could cause the wire to melt or, in the case of the LHC, quenching of the superconducting magnets. To prevent any uncontrolled movements of the forks a magnetic locking device has been designed. The concept is shown in Fig. 1.3.2. It consists of a magnetic circuit in two parts. The part outside vacuum is composed of a permanent magnet and an electrical coil and the in-vacuum part contains a ferromagnetic piece fixed to the shaft. When current runs through the electrical coil the magnetic field of the permanent magnet is cancelled allowing the shaft to rotate freely.

1.3.2 Objectives

The present thesis focuses on the most critical mechanical components in the new fast wire scanner design. The new design of the wire scanner, with the rotating parts of the motor and resolver in vacuum requires a motor housing to separate the vacuum from the atmosphere. The housing needs to be thin to fit within the maximum allowed air gap (approximately 0.8 mm) between the rotor and stator of the electric motor. Therefore a study is done to determine what minimum thickness of the motor housing is required. The housing is composed of two different parts. One part surrounds the rotor of the motor and the other part the rotor of the resolver. The critical buckling load is computed for different thicknesses of the motor housing, in order to determine the required thickness. The motor housing is made of an austenitic stainless steel, AISI 316L.

Moreover, the material that best meets the requirements of the shaft has to be selected. The material must of course be compatible with the wire scanner's operating environment. It must be ultra-high vacuum (UHV) compatible, radiation resistant, non-magnetic and must be able to resist a bake-out at 250°C for 24 hours (which is done to remove gas molecules that could otherwise disturb the beam vacuum). The choice of material should maximise the stiffness of the shaft and make sure that the vibrations are kept small. It is also essential that the shaft is machinable so that it, first of all, is possible to manufacture. Secondly, the other components of the shaft assembly must be attachable to the shaft.

The shaft assembly consists of a shaft with three rotors (one for the motor, one for the magnetic lock and one for the resolver), two bearings on opposite sides of the shaft, two forks to hold the wire as well as an optical disc to measure the position of the wire. A schematic drawing (not including the magnetic lock) of the shaft is shown in Fig. 1.3.3.

The shaft needs to withstand the stress it is subjected to due to the different loads acting on it. The design of

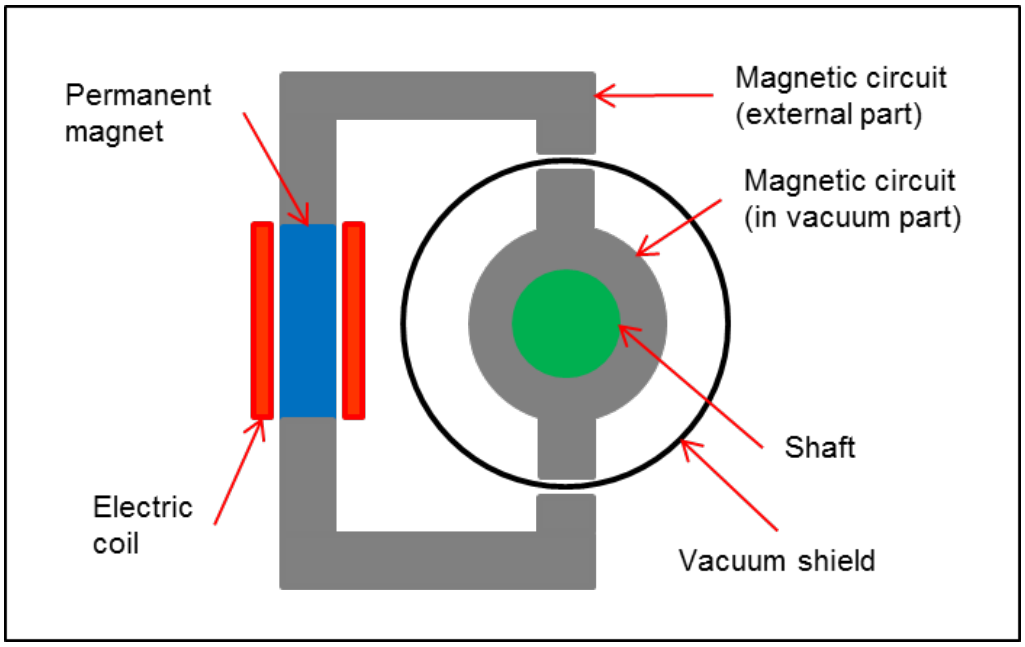

Figure 1.3.2: Schematic drawing the magnetic lock which prevents any unplanned movements of forks and wire [9].

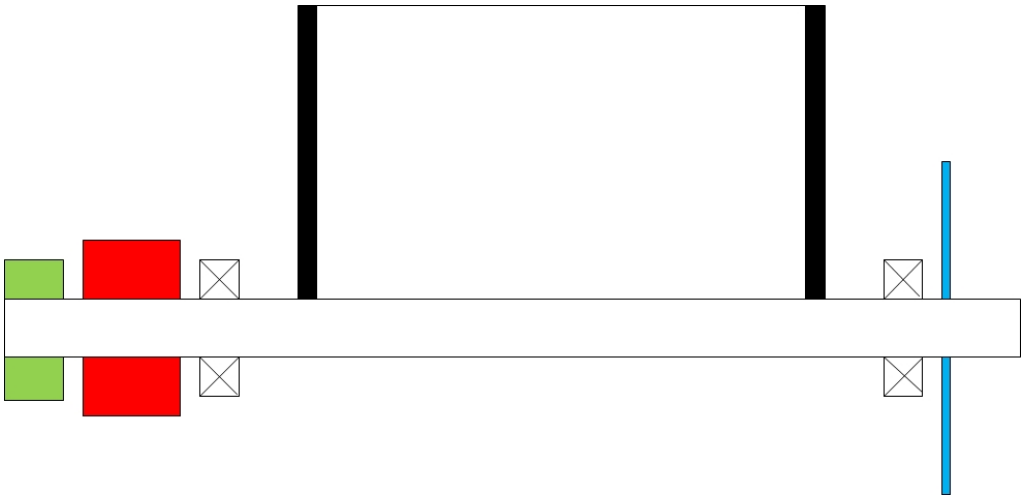

Figure 1.3.3: Schematic drawing of shaft assembly. The components mounted on the shaft are (from the left): resolver, electric motor, bearing, forks, bearing and optical disc.

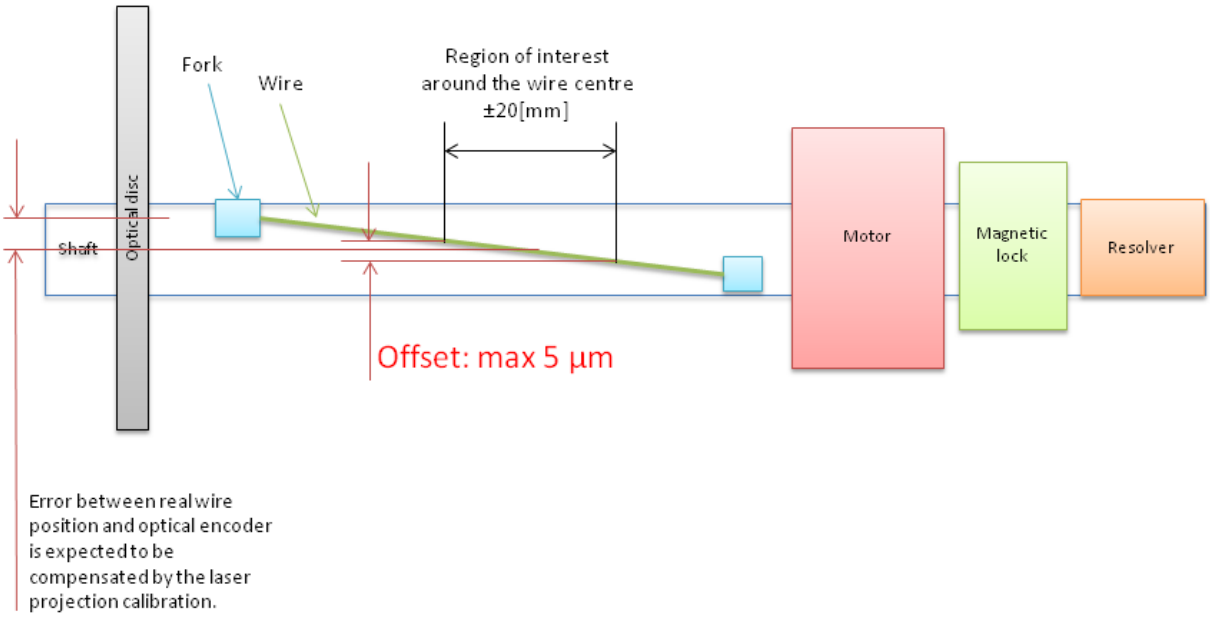

Figure 1.3.4: Precision requirement of the new fast wire scanner.

the shaft must also be such that it ensures sufficiently small deformations in torsion. The maximum allowed deformation is defined by the maximum tolerated offset of the wire relative to its centre position. Since the wire scanner is calibrated with respect to the centre of the wire this offset has to be limited to 5 μm within a distance of $\pm$20 mm from the wire centre to reach the precision requirements. This is hereafter referred to as the region of interest and represents the part of the wire that will be hit by the beam during a scan. Figure 1.3.4 illustrates this requirement. Further, the shaft needs to be hollow to facilitate space for cables to pass through it and its inertia should be kept small to minimise the power needed from the motor. The operating condition which is studied is at maximum acceleration, which corresponds to the condition where the highest deformation and stresses are achieved.

The forks are mounted on the shaft and their function is to hold the wire. The forks need to be stiff in order not to induce excessive vibrations in the wire and at the same time must be kept light to minimise the inertia of the system. Since the precision requirements for the new wire scanner have been tightened at the same time as the scanning speed has been increased the forks need to be carefully optimised.

1.3.3 Boundaries

In the earlier phases of the wire scanner project, the actuator and control systems as well as the optical encoder system have been well developed [7, 10] and are not included as part of this thesis. Furthermore, the bearings have not been treated in this paper. The integration of all parts in the final assembly is also outside the scope of this thesis. This thesis concentrates on simulation driven analysis of the treated components and an experimental evaluation is not conducted due to time constraints.

2 Theory

In this chapter the theoretical background to the buckling analysis and the topology optimisation that are performed in the present thesis is presented.

2.1 Buckling

Slender structures, *i.e.*, where at least one characteristic dimension is significantly smaller than the other dimensions are in general prone to structural instability, or buckling, if they are subjected to compressive loading [11]. Examples of such structures are thin plates and slender beam structures, as well as thin shells such as the vacuum motor housing treated in this thesis.

Buckling is manifested as a sudden deformation, which can be of significant magnitude. Depending on the structure's configuration buckling may cause limited inconvience or lead to complete structural collapse. Mathematically the buckling problem is represented by a bifurcation in the "solution path". This means that there are several equilibrium paths on the load-deflection curve, corresponding to several equilibrium configurations of the structure, and hence instability [11]. This is characterised by an eigenvalue problem. In ANSYS [12], which is used in this thesis, this eigenvalue problem is expressed according to Eq. 2.1.1 [13].

$$([K] + \lambda_{\mathrm{i}}[S])\psi_{\mathrm{i}} = 0 \tag{2.1.1}$$

where K denotes the stiffness matrix, S the stress stiffness matrix , λ the eigenvalues (load multipliers) and ψ the eigenvectors. When the load multipliers have been solved for, the reference load is then multiplied by the load multiplier to obtain the buckling load.

2.2 Structural optimisation

In topology optimisation of solid structures the goal is to find the optimal material distribution in a structure [14]. This includes determining the locations of holes and the connectivity of the material in the structure. The only known features of the problem are the applied loads, the support conditions, the bounds for the shape of the structure and possibly prescribed topological regions, such as a hole for a pipe. Topology optimisation methods are well established for minimum compliance (*i.e.*, maximum stiffness) problems with a prescribed total mass, or volume, of the structure [14]. This yields a structure with maximum stiffness for the prescribed loads and boundary conditions. The structure is modelled with a finite element (FE) mesh and evaluated using the finite element method. The initial topology has an evenly distributed mass over the design domain and is then gradually changed during an iterative procedure to create regions with maximum density and void regions [14]. In the end, a topology with either filled element volume (material) or void (no material) should remain, rendering the problem discrete.

However, in order to use a strategic search (mathematical programming) for the optimal topology the optimisation problem needs to be modelled with a continuous function [14]. This is done by assigning a continuous density function to each element. The minimum value of this function is zero, representing void material, and the maximum value is one and corresponds to a filled element. Elements with intermediate densities are unwanted in the final design, but they are necessary to give a continuous optimisation process [14].

2.2.1 Objective function

The minimising problem is formulated mathematically as [15]:

$$\min : c(\mathbf{x}) = \mathbf{U}^{\mathbf{T}}\mathbf{K}\mathbf{U} = \sum_{e=1}^{N} E_{\mathrm{e}}(x_{\mathrm{e}})\mathbf{u}_{\mathrm{e}}^{\mathbf{T}}\mathbf{k}_{\mathrm{e}}\mathbf{u}_{\mathrm{e}} \tag{2.2.1}$$

Subject to:

$$\begin{aligned} V(\mathbf{x})/V_0 &= f \\ \mathbf{KU} &= \mathbf{F} \\ \mathbf{0} \leq \mathbf{x} &\leq \mathbf{1} \end{aligned} \tag{2.2.2}$$

where $c(\mathbf{x})$ is the structure's compliance, $\mathbf{U}$ and $\mathbf{K}$ are the global displacement vector and global stiffness matrix, respectively, and $\mathbf{F}$ is the external force vector. The element displacements and stiffnesses are denoted $\mathbf{u}_\mathrm{e}$ and $\mathbf{k}_\mathrm{e}$. The vector of design variables (in this case the element densities) is denoted $\mathbf{x}$ and $V(\mathbf{x})$ is the total volume occupied by the non-zero density elements and V_0 is the total volume of the design domain.

The Young's modulus of each element is assigned using the following formula [15]:

$$E_\mathrm{e}(x_\mathrm{e}) = E_\mathrm{min} + x_\mathrm{e}^p(E_0 - E_\mathrm{min}), \qquad x_\mathrm{e} \in [0,1] \tag{2.2.3}$$

where E_0 is the Young's modulus of the material and E_min is a small elastic modulus used for the void regions in order to avoid a singular stiffness matrix in the FE calculations. The penalty factor, p, is introduced to ensure that a black-and-white solution is obtained (*i.e.*, completely void or completely filled elements). The penalty factor is chosen as a number larger than one and it enhances the effect of a large or small density, hence pushing the solution to either a filled or void element.

2.2.2 Optimisation scheme

An optimising scheme based on the Optimality Criteria (OC) [15] method is used. The design variables (densities) are updated using the following scheme:

$$x_\mathrm{e}^\mathrm{new} = \begin{cases} \max(0, x_\mathrm{e} - m) & \text{if } x_\mathrm{e}B_\mathrm{e}^\eta \leq \max(0, x_\mathrm{e} - m) \\ \min(1, x_\mathrm{e} + m) & \text{if } x_\mathrm{e}B_\mathrm{e}^\eta \geq \max(1, x_\mathrm{e} - m) \\ x_\mathrm{e}B_\mathrm{e}^\eta & \text{else} \end{cases} \tag{2.2.4}$$

where m is a positive move limit, η is a numerical damping exponent (set to 0.5) and B_e is obtained as [15]:

$$B_\mathrm{e} = \frac{-\frac{\partial c}{\partial x_\mathrm{e}}}{\lambda \frac{\partial V}{\partial x_\mathrm{e}}} \tag{2.2.5}$$

The Lagrangian multiplier, λ, needs to be chosen such that the volume constraint is satisfied. A bisection algorithm can be used to achieve this [15]. The sensitivities of the objective function, c, and volume, V, with respect to the design variable, x_e, are computed using [15]:

$$\frac{\partial c}{\partial x_\mathrm{e}} = -p x_\mathrm{e}^{p-1}(E_0 - E_\mathrm{min})\mathbf{u}_\mathrm{e}^\mathbf{T}\mathbf{k}_0\mathbf{u} \tag{2.2.6}$$

$$\frac{\partial V}{\partial x_\mathrm{e}} = 1 \tag{2.2.7}$$

Equation 2.2.7 is based on the assumption that all elements have unit volume [15].

2.2.3 Filtering

To ensure that a physically feasible solution is obtained some kind of filtering technique needs to be applied. The element densities are filtered according to the following equation [15]:

$$\bar{x}_\mathrm{e} = \frac{1}{\sum_{i \in N_\mathrm{e}} H_\mathrm{ei}} \sum_{i \in N_\mathrm{e}} H_\mathrm{ei} x_\mathrm{i} \tag{2.2.8}$$

where H_ei is a weight factor determined by [15]:

$$H_\mathrm{ei} = \max(0, r_\mathrm{min} - \Delta(e,i)) \tag{2.2.9}$$

The filtering radius is given by r_min and Δ denotes the distance between the centre of two elements. It should be noted that the original densities, x, lose their physical meaning after filtering, meaning that the filtered densities, $\bar{x}_\mathrm{e}$, should be presented as the solution [15].

2.2.4 Explicit analytical solutions

For statically determined structures, explicit analytical solutions for the optimal shape can be found. Minimising the compliance for a given mass is equivalent to keeping the ratio between sub-region energy and sub-region mass constant in all the design sub-regions [16]. The stress energy, U_σ, of a sub-region (ranging from a to b) for pure bending with a simple beam model and linear elasticity is expressed as:

$$U_\sigma = \int_a^b \frac{M^2}{2EI}\mathrm{d}x = \int_a^b \frac{M^2}{2E\alpha^2 A^2}\mathrm{d}x \tag{2.2.10}$$

Here a simple relation for the cross-sectional moment of inertia, $I = \alpha^2 A^2$, is assumed, where α is a constant for each cross section. The bending moment is denoted M, E is the Young's modulus and x is the length coordinate. With the mass

$$m = \int_a^b \rho A \mathrm{d}x \tag{2.2.11}$$

and the optimality criterion

$$(\mathrm{d}U_\sigma/\mathrm{d}A) = \tilde{C}(\mathrm{d}m/\mathrm{d}A) \tag{2.2.12}$$

the following expression is obtained for the optimal shape [16]:

$$\begin{gathered} \int_a^b \left(\mathrm{d}\left(\frac{M^2}{2E\alpha^2 A^2}\right)/\mathrm{d}A\right)\mathrm{d}x = \tilde{C}\int_a^b (\mathrm{d}(\rho A)/\mathrm{d}A)\mathrm{d}x \Rightarrow \\ A = C\left(\frac{\int_a^b M^2 \mathrm{d}x}{b-a}\right)^{1/3} \Rightarrow A = CM^{2/3} \quad \text{for} \quad (b-a) \to 0 \end{gathered} \tag{2.2.13}$$

where ρ is the material density and A the cross-sectional area, while $\tilde{C}$ and C are constants.

3 Method

This chapter describes the procedures for the analyses of the different components that are carried out in this project.

3.1 Motor housing

The motor housing is analysed using the FE program ANSYS. The geometry is built up in ANSYS Design-Modeler by generating a thin cylindrical shell in three parts, see Fig. 3.1.1. The shell geometry is modelled as being perfectly cylindrical and has constant wall thickness. After that a pre-stress analysis is made using a static structural analysis with linear elastic material properties. A fixed support is used for the open end and an external pressure corresponding to the atmospheric pressure of 0.1 MPa is applied normal to all external surfaces. The results from the pre-stress analysis are then used as input to a linear buckling analysis. The linear buckling analysis solves an eigenvalue problem and is performed to give a first estimation of the load the structure can withstand before buckling.

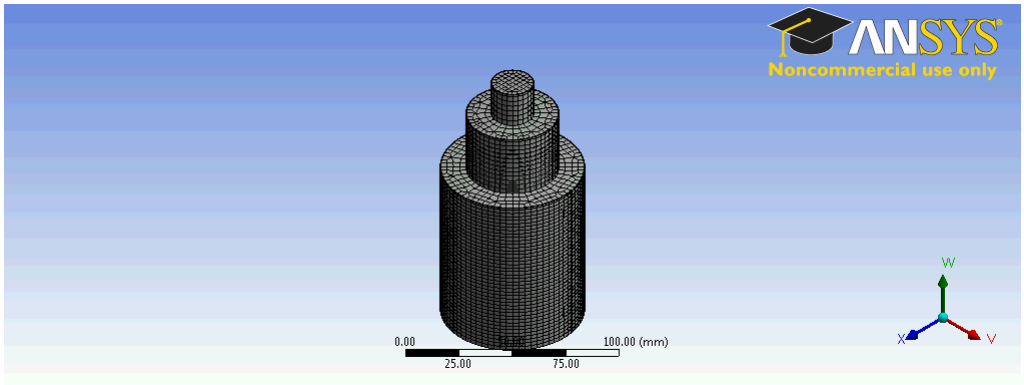

Figure 3.1.1: Motor housing mesh, with a motor length of 50 mm, as modelled in ANSYS.

Since generally linear buckling theory overestimates the buckling load [11], especially for cylindrical shells, a non-linear simulation is also run to give a better approximation. In the non-linear analysis, the mode shape from the linear buckling calculation is used to perturb the mesh, thereby introducing geometrical imperfections [17]. This is done by multiplying the results for the deformation obtained from the linear buckling analysis by a factor which renders the maximum deformation to be approximately equal to the manufacturing tolerance for the cylindricity of the shell (0.1 mm on the diameter). The motivation for using the linear buckling mode shapes to perturb the mesh is that it is assumed to create a weaker structure (and hence a worst-case scenario) if it follows the shape of the predicted linear buckling modes.

The mesh perturbation is performed by taking the deformation results from the linear buckling analysis (which are normalised to 1 mm) and multiplying by 0.1 in an input file to ANSYS Mechanical APDL. This in turn is then transferred to the Finite Element Modeler module, where the perturbed mesh is generated, and it is then transferred to a new static structural analysis. It is verified that the mesh is properly deformed by setting the multiplication factor to 10, instead of 0.1, so that a visible deformation can be displayed in the Finite Element Modeler.

The perturbed mesh is then used in a static structural analysis in ANSYS using large deflection effects and non-linear material properties. A bi-linear isotropic hardening is used in ANSYS to approximate the plastic behaviour of the 316L austenitic stainless steel. The tangent modulus is derived by fitting a line to a curve obtained from [18] in the range of the strains that are relevant in the analysis. The non-linear analysis is then conducted by successively increasing the pressure load and studying the load vs. deformation curve to establish at what load non-linear buckling occurs. This is when the deformation rate increases rapidly for small load steps.

Simulations are run for wall thicknesses of 0.25 mm, 0.3 mm and 0.4 mm for the part of the shell that is in the motor (*i.e.*, the part with the largest diameter). Also different lengths of the motor part are studied to determine how sensitive the buckling load is to the length. Lengths of 50 mm, 70 mm and 90 mm are simulated.

The elastic radial deformation under an external pressure corresponding to the operating condition (0.1 MPa) is also computed. This is especially important since the air gap between rotor and stator of 0.8 mm is small. Therefore it needs to be determined if the deformations are small enough not to interfere with the motor rotor during operation.

3.2 Material selection for shaft

The material selection procedure follows the strategy described by Michael Ashby in [19]. Using this strategy, first, the constraints and objectives for the material choice are identified. Secondly, a screening is done to filter out all materials that do not fulfil the constraints. After that, the material indices (based on the material properties) that optimise performance are derived. Subsequently, the materials are ranked according to the derived indices. Finally, additional information on the top candidates from the ranking is found in what is referred to as the documentation phase before a final selection of the most suitable material is made.

3.2.1 Constraints and objectives

The shaft is subjected to some constraints, mainly related to its operating environment. It must also meet a couple of performance objectives. All identified constraints are listed below.

- The material of the shaft must be ultra-high vacuum (UHV) compatible. The highest requirement in this respect is the LHC beam vacuum which is in the order of 10^{-8} Pa. The outgassing rate under these conditions should be below 10^{-9} Pa m^3 s^{-1} [8] .
- The shaft should be non-magnetic not to interfere with the particle beam.
- It has to be strong enough not to fail or yield under the applied loads.
- The shaft must be machinable and other components must be possible to attach to it.
- It has to resist a bake-out at 250℃ for 24 hours to remove any residual gas molecules from its surface.
- The material must be radiation resistant. The maximum cumulative ionising radiation on the component is 20 kGy over the expected lifetime of ten years [7].

The objectives in terms of shaft performance are to minimise the deformations in torsion and bending as well as to minimise the vibrations of the shaft.

3.2.2 Screening

As a first stage in the screening process, different material groups (such as polymers and metals) are compared to see if some material groups can be excluded completely. After that, the constraints listed in Sec. 3.2.1 are used to screen out unsuitable materials in the remaining material groups.

3.2.3 Derivation of material indices

The material indices that optimise the structure with respect to the objectives presented in Sec. 3.2.1 are derived by looking at the governing equations for the properties of the structure that should be optimised. One objective is to maximise the values of the eigenfrequencies, to obtain a favourable vibrational response of the shaft. The values of the eigenfrequencies, ω_n, for torsional vibrations depend on the relation shown in Eq. 3.2.1.

$$\omega_\mathrm{n} \propto \sqrt{\frac{GK}{J}} \tag{3.2.1}$$

where G is the shear modulus, K the geometric shape factor and J the mass moment of inertia. The next step is to eliminate the variables which do not depend on the material. This is done inserting the expressions for a hollow cylinder in Eqs. 3.2.2 through 3.2.5 into Eq. 3.2.1.

$$K = \frac{\pi}{2}(r_{\mathrm{o}}^4 - r_{\mathrm{i}}^4) \tag{3.2.2}$$

$$J = \frac{m}{2}(r_{\mathrm{o}}^2 + r_{\mathrm{i}}^2) \tag{3.2.3}$$

$$m = \rho A L \tag{3.2.4}$$

$$A = \pi(r_{\mathrm{o}}^2 - r_{\mathrm{i}}^2) \tag{3.2.5}$$

where r_{o} and r_{i} denote the outer and inner radius, respectively, m the mass and ρ the density, while A is the cross-sectional area of a hollow cylinder and L represents the length of the shaft. When these equations are substituted into Eq. 3.2.1, Eq. 3.2.6 is obtained.

$$\omega_{\mathrm{n}} \propto \sqrt{\frac{G}{\rho L}} \tag{3.2.6}$$

Since the length of the shaft is not material dependent, the parameter that needs to be maximised is G/ρ. Similarly, the material indices for the longitudinal vibrations can be derived from the relation in Eq. 3.2.7.

$$\omega_{\mathrm{n}} \propto \sqrt{\frac{EI}{\rho A}} \tag{3.2.7}$$

where E is the Young's modulus of the material and I the area moment of inertia. The area moment of inertia for a hollow cylinder is written:

$$I = \frac{\pi}{4}(r_{\mathrm{o}}^4 - r_{\mathrm{i}}^4) \tag{3.2.8}$$

Inserting Eqs. 3.2.8 and 3.2.5 into Eq. 3.2.7 results in

$$\omega_{\mathrm{n}} \propto \sqrt{\frac{E(r_{\mathrm{o}}^4 - r_{\mathrm{i}}^4)}{\rho(r_{\mathrm{o}}^2 - r_{\mathrm{i}}^2)L}} \tag{3.2.9}$$

Due to that r_{i}, r_{o} and L only depend on the geometry this means that the material index that needs to be optimised is E/ρ.

The same procedure is followed for the static deformations (due to the acceleration of the shaft) in torsion and bending. In torsion, the twisting angle, ϕ, is computed using Eq. 3.2.10.

$$\phi = \frac{M_{\mathrm{v}} L}{GK} \tag{3.2.10}$$

Here, the twisting moment, M_{v}, is load dependent and L and K are geometry dependent. This means that in order to minimise the torsional deformation, G needs to be maximised. The transversal deflection, w, due to bending varies according to Eq. 3.2.11.

$$w \propto \frac{1}{EI} \tag{3.2.11}$$

Hence, E needs to be maximised in order to minimise the deformation.

3.2.4 Ranking

In this step, the values of the material indices for the remaining materials are displayed in a scatter plot to create a clear illustration of which materials meet the objectives in the best way. These plots are then used to rank the materials based on the derived indices.

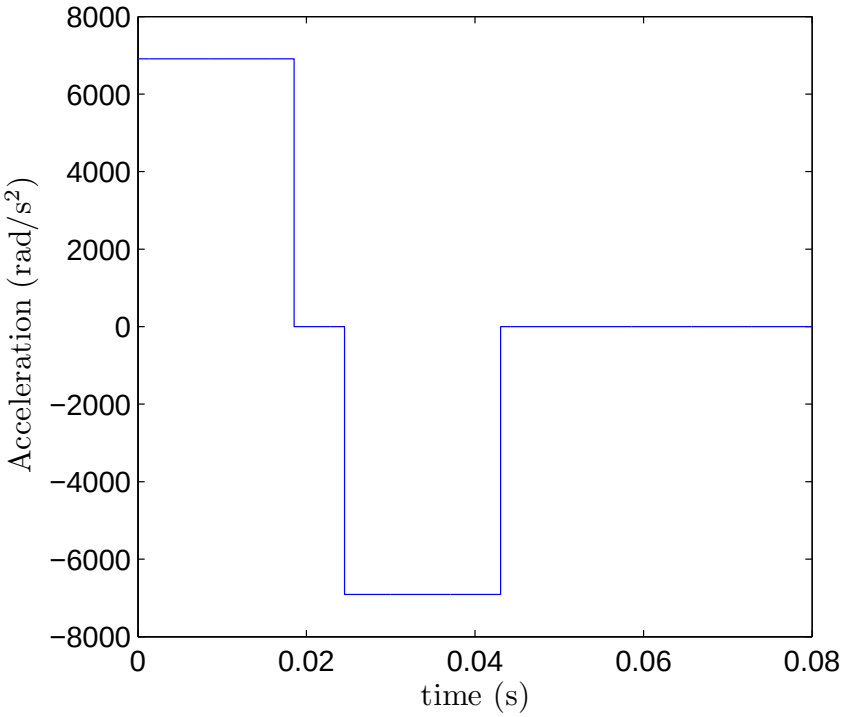

Figure 3.3.1: Square acceleration profile imposed on the shaft.

3.2.5 Documentation

The documentation phase serves to obtain additional information on the top candidates to determine if there are other details, such as health or environmental issues, which are important in the final decision other than those covered in the previous steps. After this, a final selection of material is made taking into consideration the ranking of the material indices and the additional information which is gathered in the documentation phase.

3.3 Dimensioning of shaft

The shaft is analysed using ANSYS. The angle of twist and the equivalent stress in the shaft are evaluated by imposing two different angular accelerations, 6727 rad/s^2 and 15135 rad/s^2, on the shaft. The two values of the acceleration correspond to a constant acceleration to wire scanning speeds of 20 m/s and 30 m/s, respectively. The square acceleration profile used for the lower of the two accelerations is shown in Fig. 3.3.1. The analysis using the higher acceleration (leading to a wire speed of 30 m/s using constant acceleration) is performed to study how the shaft performs when it is subjected to higher loads, which can be present if other, smoother, acceleration profiles are used.

In order to simulate the shaft, first, the magnitudes of the twisting loads are calculated. This is done to create a computationally efficient analysis. The rotationally symmetric components mounted on the shaft (*i.e.*, the rotors, bearings and optical disc) are assumed to be perfectly centered in the analysis. Therefore the loads appearing on the shaft when these components are accelerated can be translated into an opposing torque. The opposing torques, M, are calculated from the mass moment of inertia, J, of the different components and the angular acceleration, $\dot{\omega}$, according to Eq. 3.3.1.

$$M = J\dot{\omega} \tag{3.3.1}$$

The mass moments of inertia for the rotor and resolver are obtained from the data sheets for the two components. The bearings used in the calculation are the same as those installed in the test bench that was used for the tests of the motor [8] and therefore those values are used as input. The inertias of the disc, disc holder and

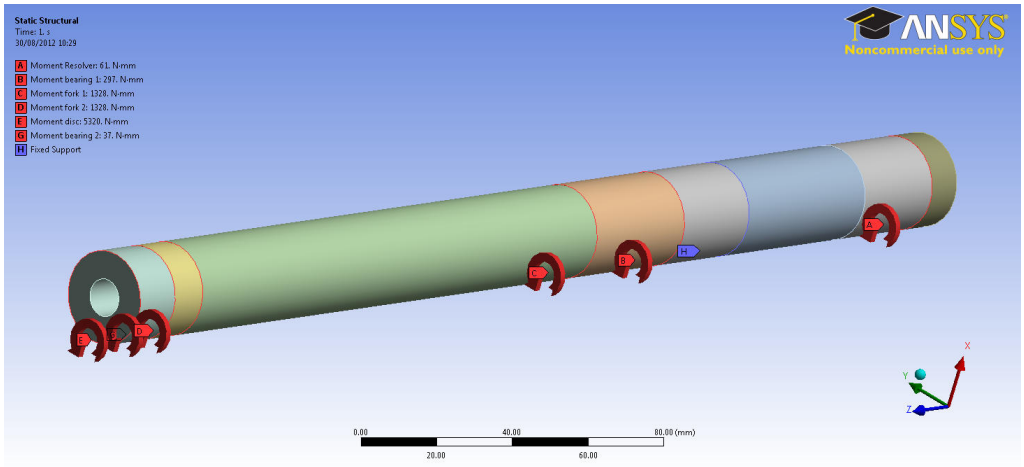

Figure 3.3.2: Shaft geometry with the disc located to the left in the picture.

shaft are calculated using Eq. 3.3.2, where r denotes the distance from the axis of rotation and m the mass. Two soda-lime glass discs of different thickness (1 mm and 3 mm, respectively) are simulated due to that the final selection of the optical disc had not been made at the time of these computations.

$$J = \int_{r_1}^{r_2} r^2 \, \mathrm{d}m \tag{3.3.2}$$

The forks used in the shaft simulation are approximated as two solid steel triangles joined perpendicularly. This is to achieve a relatively heavy fork design and thereby a worst-case scenario for the shaft twist. Since the loads from the forks are eccentric, there will be both a reaction moment and a reaction force acting on the shaft due to the acceleration. The equations of motion for the fork are:

$$\begin{aligned} M_\mathrm{r} &= J_\mathrm{fork}\dot{\omega} \\ F_\mathrm{r} &= m_\mathrm{fork}a = m_\mathrm{fork}\bar{r}\dot{\omega} \end{aligned} \tag{3.3.3}$$

The reaction force can also be converted to a moment, since the shaft is thin, by multiplying the force with the shaft's outer radius.

$$M_\mathrm{r,conv} = F_\mathrm{r} r_\mathrm{o} \tag{3.3.4}$$

The total torque acting on the shaft from the forks therefore becomes:

$$M_\mathrm{f} = M_\mathrm{r} + M_\mathrm{r,conv} \tag{3.3.5}$$

There will also be a bending of the shaft caused by the rotational velocity but this is neglected in this analysis since the precision requirement comes from the shaft twist (see Fig. 1.3.4). Furthermore, the small amount of bending deformation that will occur will largely be in the direction of the beam during the scan, which does not create any further inaccuracies in the measurements.

The shaft geometry is built in ANSYS DesignModeler by stacking several hollow cylinders on top of each other. This is done in order to create edges where the torsional moments can be applied. The opposing torque of each component mounted on the shaft is applied on the edge corresponding to each component's respective position. A picture of the shaft geometry, with the torques applied, is shown in figure 3.3.2. A fixed support boundary condition is applied at the motor position to specify the location where the acceleration is applied in the real system.

The system is accelerated with the two different accelerations (6727 rad/s^2 and 15135 rad/s^2) to create the loading case corresponding to accelerating the shaft. The values of the inertia and resistant torques used in the simulations are shown in Tab. 3.3.1. The results for the deformation are obtained along the outer circumference of the shaft at the two fork positions. From this, the fork tip deflections (assuming rigid forks), $\delta_\mathrm{fork,i}$, can be

Table 3.3.1: Inertia and resistant torque values used in the shaft simulations.

Component	J (kgm^2)	M (Nm) 6727 rad/s^2	M (Nm) 15135 rad/s^2
Bearing 1	$1.96 \cdot 10^{-5}$	0.132	0.297
Bearing 2	$2.45 \cdot 10^{-6}$	0.016	0.037
Disc 1 mm	$8.35 \cdot 10^{-5}$	0.562	1.26
Disc 3 mm	$2.51 \cdot 10^{-4}$	1.686	3.793
Disc holder	$2.68 \cdot 10^{-4}$	1.801	4.053
2 Forks	$1.76 \cdot 10^{-4}$	1.581	3.556
Resolver	$4.00 \cdot 10^{-6}$	0.027	0.061
Rotor	$3.40 \cdot 10^{-4}$	2.287	5.146

calculated by extrapolation (since the material is linear elastic). The fork tip deflections, in turn, are then used to calculate the wire offset in the region of interest (see Fig. 1.3.4) according to Eq. 3.3.6.

$$\delta_{20\text{mm}} = (\delta_{\text{fork},2} - \delta_{\text{fork},1}) \frac{40[\text{mm}]}{d_{\text{fork}}} \tag{3.3.6}$$

where d_{fork} denotes the distance between the forks. The convergence of the solution is then continuously checked by comparing the results of two differently sized meshes.

3.4 Forks

With the emerging possibilities of using additive manufacturing (or 3D-printing) substantial design freedom is given since structures with, for example, complex internal structures can more easily be realised than with conventional manufacturing methods. Therefore topology optimisation methods are an attractive way of finding a structurally optimal shape. The optimisation is performed in 2D with the use of MATLAB and an optimisation run in 3D is performed using the commercial software Altair HyperWorks. Furthermore, a parameter correlation analysis and a goal driven optimisation are conducted in ANSYS to further improve the design. The suggested designs are then evaluated using ANSYS simulations. The structure is optimised with the objective of minimising the compliance of the fork structure. The idea behind this is to obtain as small deformations as possible during the acceleration phase of the scan in order to have small vibrational amplitudes of the wire when it crosses the beam. This will in turn keep the uncertainties of the measurements at a minimum. A further motivation for performing a minimum compliance optimisation is that methods for this are well developed in academic research (see Sec. 2.2).

3.4.1 2D topology optimisation

The optimisation is performed using a program based on top88.m [15]. This program optimises the material distribution for a 2D structure using the SIMP method described in section 2.2. The penalty factor (p in Eq. 2.2.3) is chosen as 3 and the filter radius, r_{min}, as 1.5 to obtain a black-and-white (*i.e.*, filled or empty elements) solution while still keeping the program numerically stable. The rotational loads are introduced by lumping the loads acting on each element and applying them to the degrees of freedom (in the direction of the force) of the element.

3.4.2 3D topology optimisation

A 3D topology optimisation is carried out in the program suite Altair HyperWorks, using the optimisation module OptiStruct. A parallelepiped envelope is created in ANSYS DesignModeler and then imported into HyperWorks as a step-file. The model is then meshed in HyperMesh and the optimisation is set up, defining the material (titanium in this case), boundary conditions and the rotational load. The RFORCE option is used for defining the rotational acceleration. A design constraint is put on the maximum volume fraction (0.3) and then the objective function is set as minimising the tip displacement. Another optimisation run is made using a triangularly shaped design domain. In this run more constraints are put on the design space to ensure a

physically feasible solution. The elements near the edges of the triangle are not included in the design space and instead, material filled elements are prescribed in this region.

3.4.3 Parameter correlation analysis

A parameter correlation study is set up in ANSYS based on the design suggested from the results of the optimisation for the triangular envelope in OptiStruct. This is done to determine which dimensions influence the deflection the most, and how they influence the deflection. It is also interesting to study which parameters that do not have a significant influence on the deflection since this gives an opportunity to remove material (hence lowering the inertia) without compromising the stiffness of the fork. A Spearman rank order correlation coefficient method [20] is chosen to determine the correlation.

3.4.4 Goal-driven optimisation using parameters

Another parameter study is made to find the optimal 2D shape outline of the fork. This is done by using five and ten equally distributed control points along the length of the fork and then running a goal driven optimisation in ANSYS to find the optimal shape. The optimisation module chooses design points to optimally fill the design space (*i.e.*, the range of the allowed values specified by the user) [20]. From the simulations run for these design points, a response surface is constructed by fitting the data from the simulation results using full second order polynomials [20]. The optimal designs are then found by searching for optimum points on the obtained response surface using nonlinear programming by quadratic lagrangian (NLPQL) [20].

Since the optimum points from the goal driven optimisation are achieved by surface fitting, a verification of the results are needed. This is done by carrying out simulations for the suggested design points. Furthermore simulations of some primitive designs such as a rectangular shape and a triangular shape fork are also conducted to compare their performance with the optimised shape outlines. Also an interpretation of the 2D topology optimised design (Sec. 3.4.1) is simulated in this step for the same reason.

To obtain the optimal shape for bending due to wire tension the moment distribution needs to be found in order to use Eq. 2.2.13. For a cantilever beam with a point load at the tip it is easily shown that this varies linearly along the length of the beam. The results of these studies are then combined and a suggestion of a final optimised design is developed for further analysis and verification of its performance.

3.5 Transient simulation of forks

The suggested design, based on the topology optimisation, parameter correlation analysis and goal-driven optimisation is analysed to determine its performance. In order to capture the dynamic behaviour of the forks a transient analysis of one scan is conducted. This is done by carrying out a transient structural simulation in ANSYS. The square acceleration profile of the scan (Fig. 3.3.1) is applied to the fork and from this the vibrational behaviour can be obtained. The solution method used in ANSYS is a Newmark method (which is implicit and unconditionally stable). The time-step is selected based on accuracy to resolve the three lowest eigenmodes of the fork. The mesh size is chosen with the same consideration. Therefore a modal analysis of the fork is first carried out to determine the eigenfrequencies of the lowest eigenmodes that can be excited by the present acceleration.

3.6 Transient simulation of the shaft assembly

Since the dynamics of the whole shaft assembly will contribute to the response of the forks, and because it is important to determine the offset in the region of interest (see Fig. 1.3.4) and the uncertainties of both forks, a transient analysis of the shaft assembly is carried out. The model consists of the shaft, forks, rotor and optical disc, which are the components that significantly contribute to the dynamic response, *i.e.*, they represent the highest loads on the shaft. To simulate the load a rotational acceleration and a rotational velocity are applied to the assembly. At the motor location a fixed support is applied and at the bearing locations cylindrical supports are applied which allow tangential movement of the shaft but constrain its radial and axial displacement. The dynamic behaviour using three different acceleration profiles is studied. The worst case

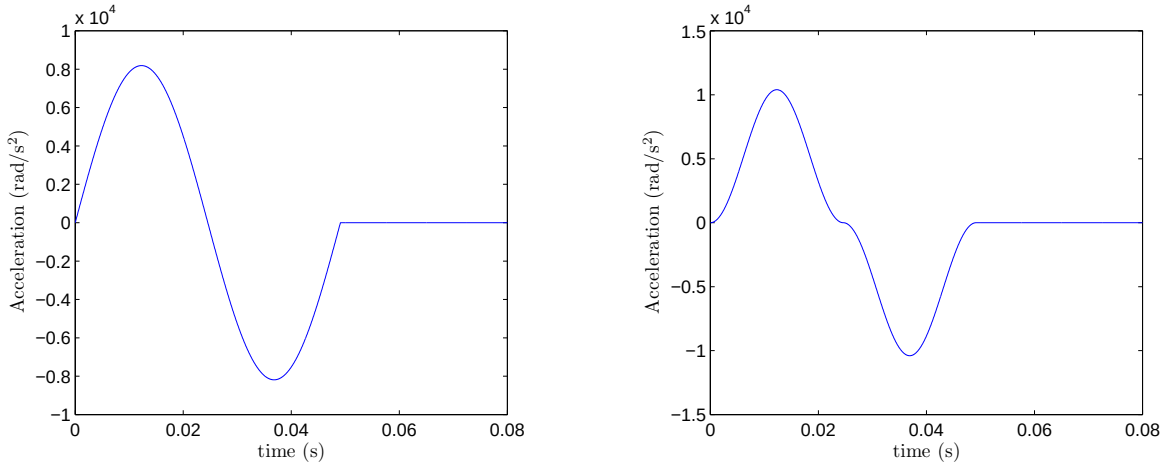

(a) Sinusoidal acceleration.

(b) Sinusoidal acceleration with constant speed through the beam.

Figure 3.5.1: Acceleration profiles foreseen for the new wire scanner, which are applied in the transient simulations of the shaft assembly.

scenario, using a constant acceleration is shown in Fig. 3.3.1 and the smoother sinusoidal acceleration profiles (however, with a higher peak acceleration) in Fig. 3.5.1 are used in this analysis. No material damping is used in the model because this simplifies the model and due to the short time-scale of one scan the damping effects are assumed to be small.

4 Results

The results of the motor housing and shaft analyses as well as the fork optimisation and the subsequent fork simulations are presented in this chapter.

4.1 Motor housing

The motor housing analysis results consisting of a linear buckling analysis followed by a non-linear analysis are shown below. The linear buckling analysis gives the shape shown in Fig. 4.1.1 as the first buckling mode. The load factor (*i.e.*, the number of times the reference load of 0.1 MPa can be increased) results for the linear buckling analysis are shown in Fig. 4.1.2. As can be seen in the figure, the load factor increases exponentially with the thickness of the shell wall, whereas the dependence on the length of the shell is weaker.

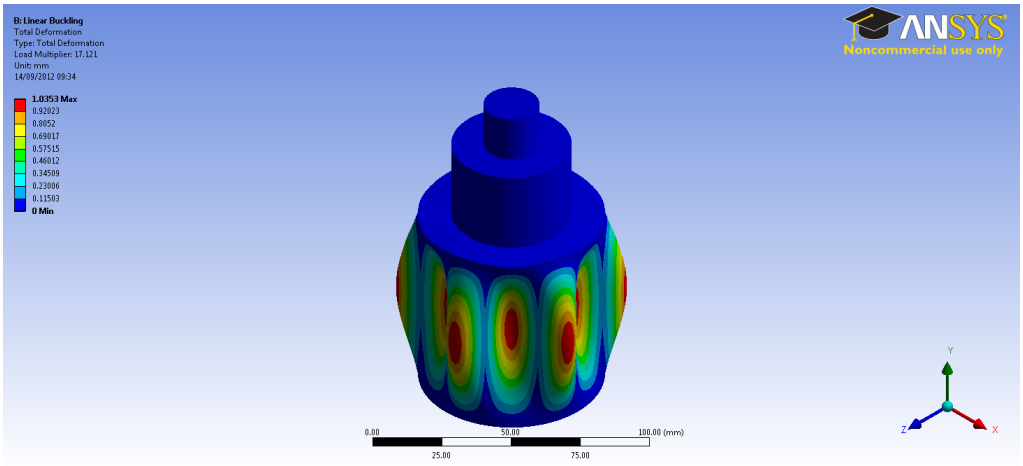

Figure 4.1.1: First buckling mode shape for the motor housing.

The non-linear buckling analysis gives a load-deflection curve such as the one shown in Fig. 4.1.3. The critical buckling load is represented by the kink in the curve, appearing at approximately 0.3 MPa. This indicates that the deformation increases rapidly for small load increases, which is a sign of buckling.

Similar load-deflection curves as the one shown in Fig. 4.1.3 are then plotted for the wall thicknesses of 0.25 mm, 0.3 mm and 0.4 mm and shell lengths of 50 mm, 70 mm and 90 mm. The critical pressures for buckling are obtained from these plots and the results are shown in Fig. 4.1.4. It can be seen that a wall thickness of 0.3 mm gives a safety factor to buckling of approximately 3. As in the linear case, the dependence on wall thickness is stronger than the dependence on shell length. The dependence on length is weaker in the non-linear analyses compared to the linear analyses. A slightly higher buckling load is obtained for the 0.3 mm thick wall with a length of 70 mm, compared to the shell of 50 mm length. This is believed to occur because different mode shapes are obtained for the different lengths. It can also be noted that, as expected (see Sec. 3.1) the non-linear analyses predict significantly lower buckling loads than the linear simulations.

It is also important that the elastic radial deformation is small, when the structure is loaded with the atmospheric pressure (0.1 MPa), since the structure must not interfere with the rotor during operation. Table 4.1.1 displays the radial deformation obtained with different dimensions of the motor housing. The results show that the deformations are small even compared to the thin air gap of 0.8 mm in the motor. It is also evident that the radial deformation is almost independent of the shell length, in the range studied.

Together, these results lead to a decision to manufacture the motor housing with 0.3 mm wall thickness. The motivation behind this is that a safety factor of 3 is deemed sufficient. A 0.3 mm thick wall also leaves more space between the stator and the rotor of the motor than a 0.4 mm thick wall hence lowering the risk of the

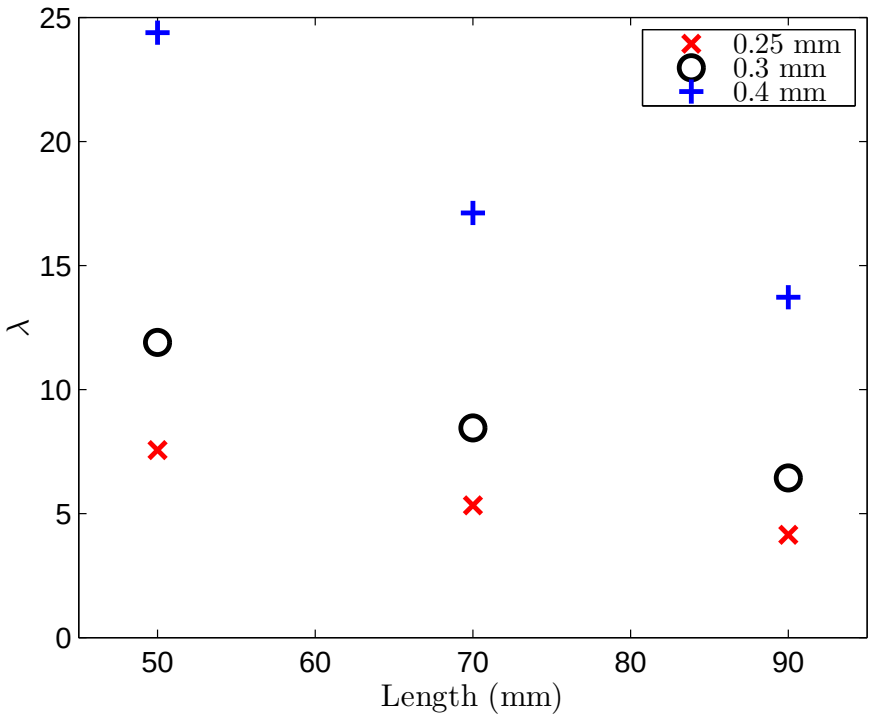

Figure 4.1.2: Load factor (λ) for different lengths and thicknesses of motor housing.

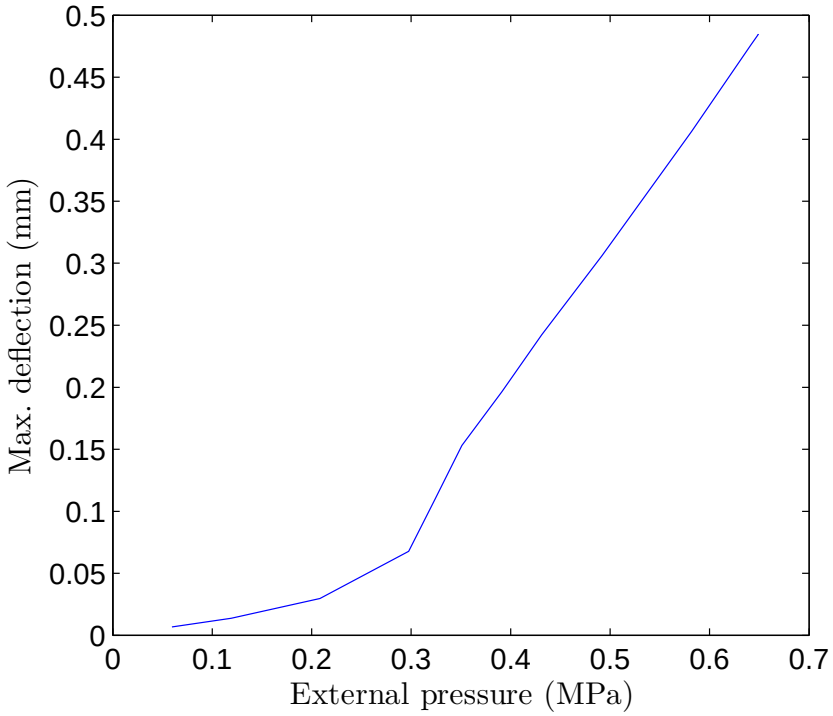

Figure 4.1.3: Load-deflection curve for a 0.3 mm thick and 50 mm long shell.

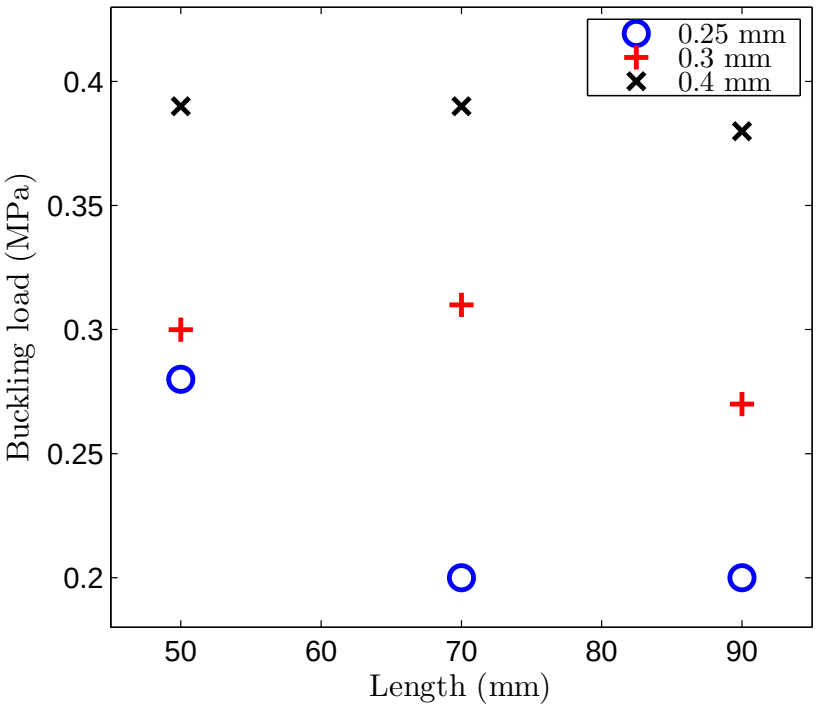

Figure 4.1.4: Collapse load for different thicknesses and length of the shell.

Table 4.1.1: Radial deformation of the motor housing under atmospheric pressure.

t (mm)	**L (mm)**	**rad.def. (mm)**
0.25	50	0.0166
0.25	70	0.0166
0.25	90	0.0166
0.3	50	0.0134
0.3	70	0.0133
0.3	90	0.0133
0.4	50	0.0092
0.4	70	0.0092
0.4	90	0.0091

rotor touching the motor housing during operation. It is decided to position the housing as close to the stator as possibly to maximise the play between rotor and housing.

4.2 Material selection for shaft

The material selection starting with the screening, and finishing with the documentation and a final decision of the material to use is presented in this section.

4.2.1 Screening

In the first step of the screening process some general properties of different material groups are identified to make a first filtering of the materials.

- Metals are stiff, easily machinable and ductile.
- Ceramics are stiff but brittle, which causes machining problems and they are sensitive to stress concentrations (*e.g.*, holes).
- Glasses are hard, brittle and sensitive to stress concentrations.
- Polymers have low melting temperatures but are easy to form.
- Composites are generally stiff and strong. They can have problems with outgassing, if they are not covered with a protective sheet (*e.g.*, aluminium).
- Elastomers do not have the required stiffness.

This list shows that metals are generally the most suitable materials for this application and therefore the other material groups are excluded from further study.

A further evaluation to determine which metals are suitable for the operational environment with ultra-high vacuum, high radiation and requirements to withstand the bakeout procedure gives the list shown in Tab. 4.2.1. For reference see [21] and [22].

4.2.2 Ranking

The parameters for the metals which meet the constraints of the operational environment are plotted in Fig. 4.2.1 and Fig. 4.2.2.

4.2.3 Documentation

The plots in Figs. 4.2.1 and 4.2.2 show that beryllium clearly outperforms all other materials. The second and third overall are molybdenum and tungsten. A literature search shows that beryllium, however, is highly toxic if dust or fumes are inhaled and can cause the lung disease berylliosis. Beryllium is rated as category 1 carcinogenic by the International Agency for Research on Cancer (IARC) [23]. Molybdenum can also cause health problems if ingested. Low levels of exposure can cause irritation to eyes and skin and higher levels can cause fatigue, headaches and joint pains [24]. Tungsten has the disadvantage that it is a very hard material which makes it difficult to machine.

Table 4.2.1: List of metals suitable for use in the wire scanner's environment.

Aluminium and alloys (Al)	Niobium (Nb)
Beryllium (Be)	Phosphor bronze (P-bronze)
Beryllium copper (Be-Cu)	Platinum (Pt)
Copper (OFHC) and copper-nickel alloys	Silver (Ag)
Gold (Au)	Austenitic stainless steels (304, 316) (SS)
Indium (In)	Titanium (Ti)
Molybdenum (Mo)	Tungsten (W)

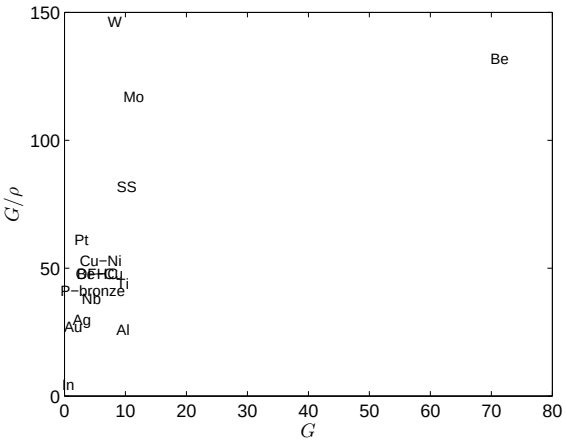

(a) Scatter plot of G vs. G/ρ.

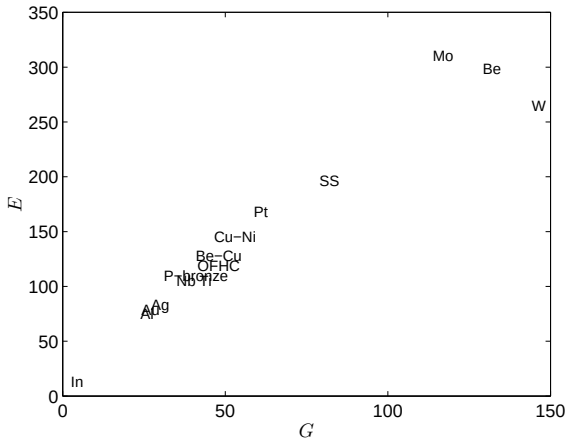

(b) Scatter plot of E vs. G.

Figure 4.2.1: Scatter plots for ranking of materials.

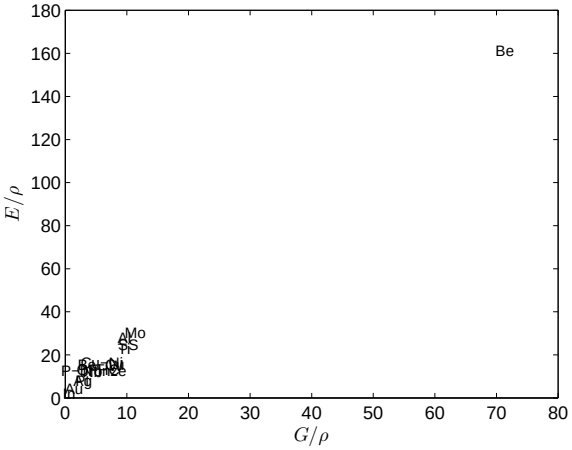

(a) Scatter plot of E/ρ vs. G/ρ.

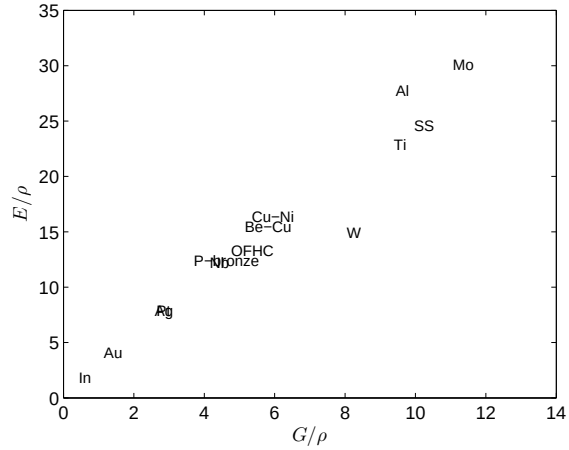

(b) Scatter plot of E/ρ vs. G/ρ with beryllium omitted.

Figure 4.2.2: Scatter plots for ranking of materials.

Table 4.3.1: Deformation in the region of interest (d) and maximum von Mises stress (σ_e) in the shaft for different outer and inner radii (r_o and r_i).

Shaft		3mm disc, 6727 rad/s^2		1mm disc, 6727 rad/s^2		3mm disc, 15135 rad/s^2		1mm disc, 15135 rad/s^2	
r_o (mm)	r_i (mm)	d (μm)	σ_e (MPa)	d (μm)	σ_e (MPa)	d (μm)	σ_e (MPa)	d (μm)	σ_e (MPa)
12.5	5	11	16.3	8.28	13.2	24.2	34.4	18	27.4
12.5	7.5	12.3	11.1	9.2	8.9	27	23.7	20.1	18.8
15	5	5.61	12.4	4.28	10.3	12	24.6	8.97	19.9
15	7.5	5.88	12.4	4.48	10.3	12.6	24.9	9.42	20.1
15	10	6.78	8.5	5.14	7.0	14.6	17.4	10.9	14.0
17.5	7.5	3.38	8.9	2.63	7.6	6.94	16.5	5.26	13.6
17.5	10	3.61	7.1	2.81	6.0	7.46	13.2	5.65	10.9
17.5	12.5	4.25	8.0	3.28	6.7	8.9	15.4	6.71	12.5

4.2.4 Final selection

Considering the drawbacks of beryllium, molybdenum and tungsten shafts, and the fact that they are rarely used as shaft materials, the best shaft material for this application is found to be the austenitic stainless steel AISI 316L. With the criteria for this application 316L outperforms the lighter materials titanium and aluminium.

4.3 Dimensioning of shaft

The results for the wire offset in the region of interest as well as the maximum equivalent stress for different shaft diameters and thicknesses of the optical disc are shown in Tab. 4.3.1 . From the results it can be seen that a shaft diameter of 35 mm is required to give the required stiffness (a maximum offset in the region of interest of 5 μm, see Fig. 1.3.4). The shaft wall can be made relatively thin, however. A shaft thickness of 5 mm is enough to keep the offset in the region of interest below the specified value of 5 μm. Further, the table shows that the stresses are low in all cases compared to the yield criteria of the stainless steel used. The largest effective stress that appears is 34.4 MPa which is significantly lower than the 200 MPa which is the yield strength. Since the maximum stresses are also significantly lower than the fatigue limit of approximately $\pm$140 MPa the risk of fatigue failure can be neglected. Therefore it is decided to manufacture a shaft with an outer radius of 17.5 mm and an inner radius of 12.5 mm.

4.4 Forks

The optimal fork design is obtained by combining the findings of the topology optimisation, the parameter sensitivity analysis and the goal driven shape outline optimisation described in Sec. 3.4. After that the performance of the optimised design is presented.

4.4.1 2D topology optimisation

The results depend strongly on the maximum allowed volume fraction as well as the settings for the penalty factor, p, and filter radius, r_{min}. Below the results are shown for a volume fraction of 0.3 (Fig. 4.4.1) and 0.15 (Fig. 4.4.2). As can be seen in the figures, a truss-structure is suggested. It is also apparent that more material is placed near the base of the fork. This is logical since the mass in this region contributes less to the mass moment of inertia than the mass near the tip. In both cases, the full width of the envelope (which is limited to 30 mm) is used for most of the fork length. The fork shape only narrows near the tip. The grey elements near the fork tip represent elements which have element densities lower than the material density. Therefore an interpretation must be made of this result to determine whether to fill these elements with material or to leave them empty.

In bending due to the wire tension, the optimal shape of a solid fork will vary with $x^{2/3}$ from the tip according to Eq. 2.2.13 (since M varies linearly). The suggested shape is illustrated in Fig. 4.4.3.

Figure 4.4.1: 2D topology optimisation for a volume fraction of 0.3. The fork base is located to the left

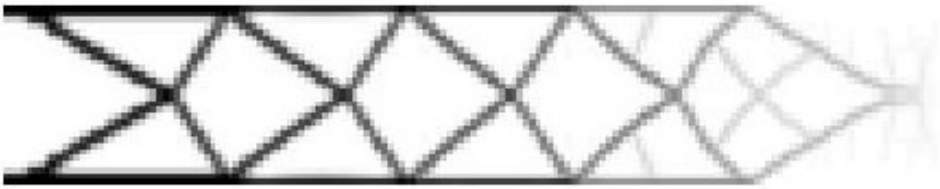

Figure 4.4.2: 2D topology optimisation for a volume fraction of 0.15. The fork base is located to the left.

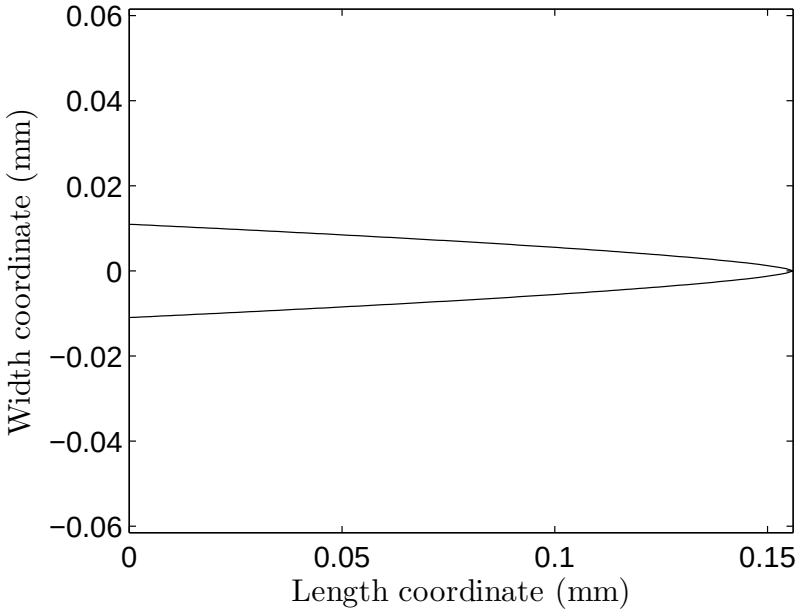

Figure 4.4.3: Suggestion of optimal shape in bending from the wire tension.

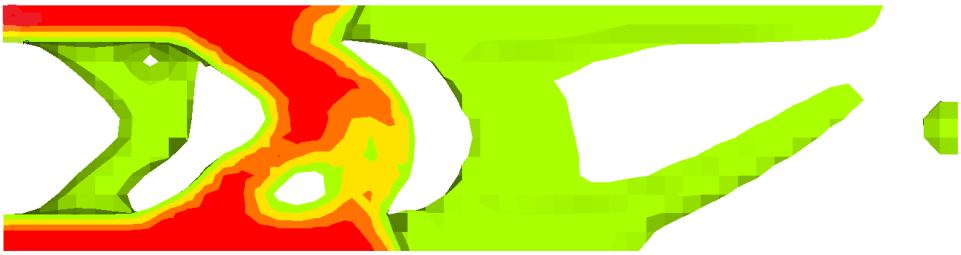

Figure 4.4.4: "Optimised" design of the fork using a parallellepiped design space.

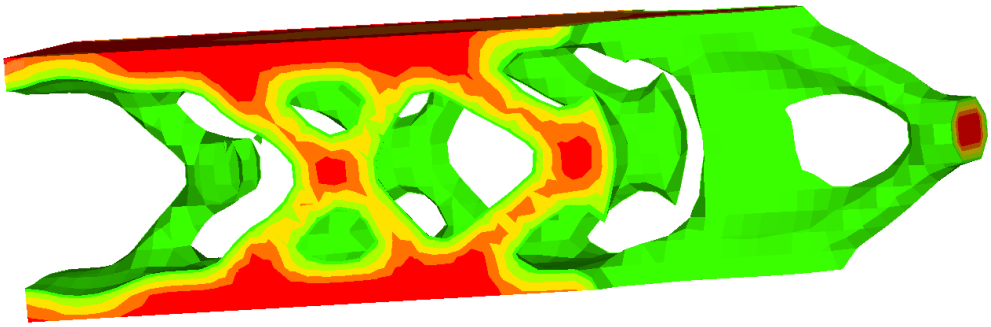

Figure 4.4.5: Optimised design of the fork when a point load is applied at the tip.

4.4.2 3D topology optimisation

In HyperWorks it was difficult to obtain a feasible solution when only few constraints were put on the use of the design space. Figure 4.4.4 shows the results obtained when the only region of prescribed material is the fork tip and when a volume fraction of maximum 0.3 is allowed. Evidently, there is no connectivity between the fork tip and the rest of the fork so the solution is unphysical. The suggested design is also asymmetric, which is not suitable for the way the wire scanner is operated (with one out-scan and one in-scan). It can be noted, however, that there is a truss-like structure for the part connected to the shaft, similar to the 2D topology optimisation.

Also a more simple case is set up, where the self-weight of the fork is not considered and the only load applied is a point force at the tip of the fork, *i.e.*, a cantilever. In this case, a feasible design is obtained, again with a truss-structure (however three-dimensional in this case) as the suggested topology, see Fig. 4.4.5. This load case is not the same as the one present when the fork is in operation but it is used to obtain a design with material connectivity to be able to compare it with the 2D optimisation in MATLAB.

An optimisation is also run where a triangular envelope for the fork is chosen. To ensure the connectivity of the fork tip with the rest of the structure, material is prescribed along the edges leading out to the tip. The resulting topology, for a volume fraction of 0.3, is shown in figure 4.4.6.

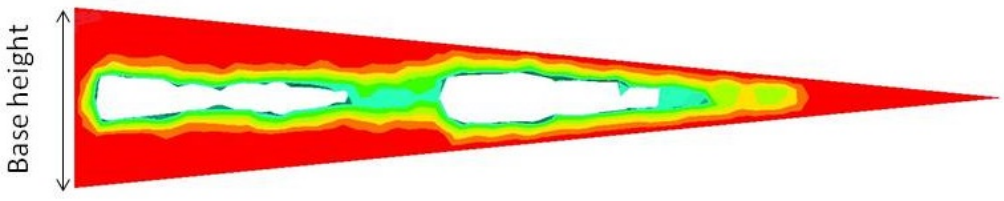

Figure 4.4.6: Optimised design with triangular design space.

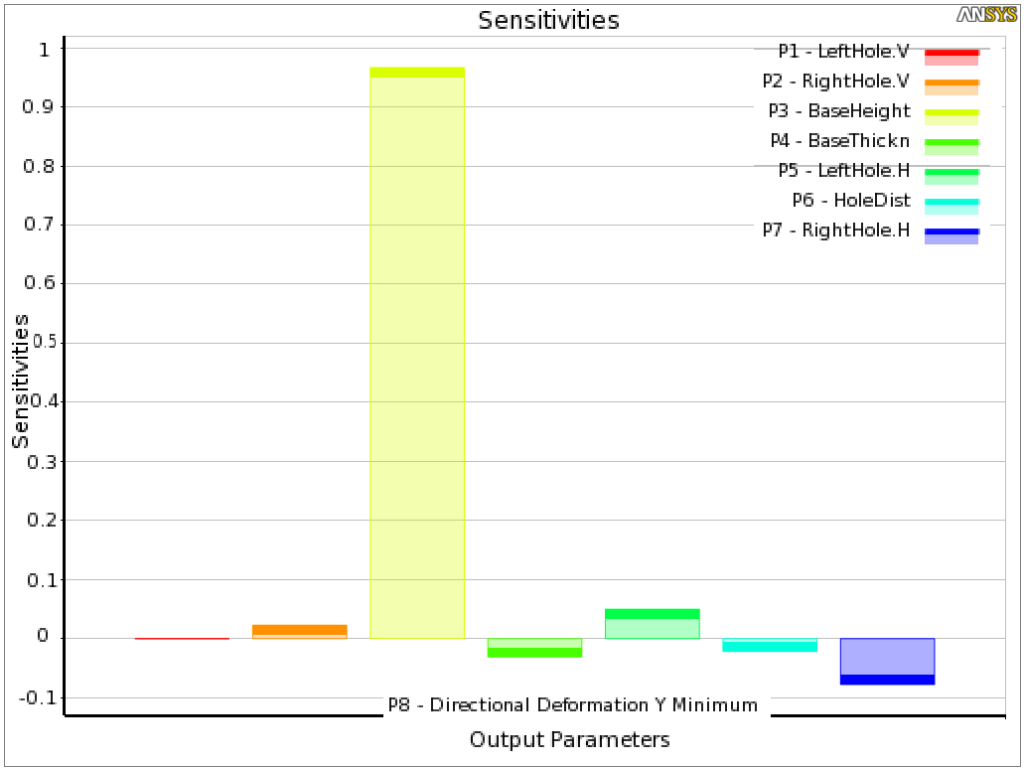

Figure 4.4.7: Parameter sensitivities. The base height (yellow) is clearly the parameter with the highest impact on tip deflection.

4.4.3 Parameter correlation analysis

The sensitivity of the tip deflection on the dimensional parameters present in the design shown in Fig. 4.4.6 is computed. The studied parameters are the horizontal and vertical dimensions of the holes, the base height (the vertical dimension of the base, see Fig. 4.4.6), the thickness of the fork material and the distance between the holes. The parameter study shows that the height of the base has the most significant influence on the fork stiffness (see Fig. 4.4.7). The positive sensitivity value of almost one shows that the tip deflection is strongly dependent on the base height where a larger value of the base height leads to a smaller tip deflection. It should be noted that the sensitivity of the tip deflection is computed for values near the dimensions obtained from the topology optimisation of the triangular domain (Fig. 4.4.6). The conclusion can still be made that keeping the base of the fork large is beneficial when a decision is made for a final optimal design. This result is also consistent with the 2D topology optimisation in MATLAB where the optimised structures used the entire width of the base.

4.4.4 Goal-driven optimisation in ANSYS

The goal-driven optimisation for the shape of the fork outline gives a shape with a wide geometry for the half of the fork closest to the base and after that the fork narrows towards the tip. The different suggested designs using 5 control points and 10 control points, evenly distributed along the fork length in both cases, are shown in Figs. 4.4.8 and 4.4.9.

4.4.5 ANSYS simulations for optimised designs

ANSYS simulations are carried out for a selection of optimised designs, to study which designs perform the best. The results from the simulations and the corresponding figures are shown in Tab. 4.4.1.

Table 4.4.1 shows the predicted tip deflections from the response surface compared with the simulated results for the specific design points. It is shown that the shape outline from the optimisation using 10 control points is the best of the solid configuration. Even better performance is shown by the truss structure inspired by the

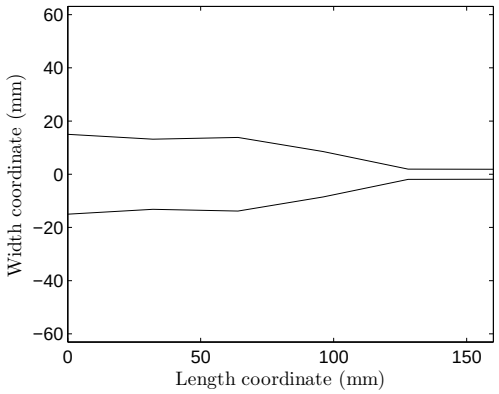

(a) First suggestion using 5 control points.

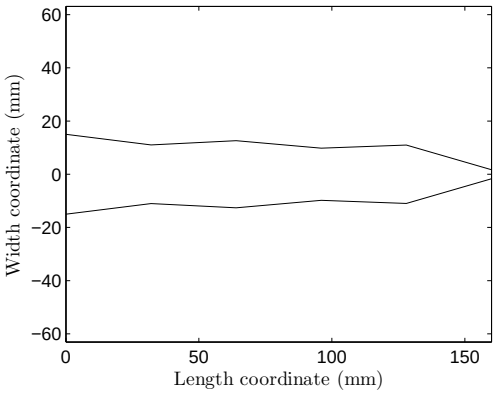

(b) Second suggestion using 5 control points.

Figure 4.4.8: Optimal shape outlines for a 2D structure without holes.

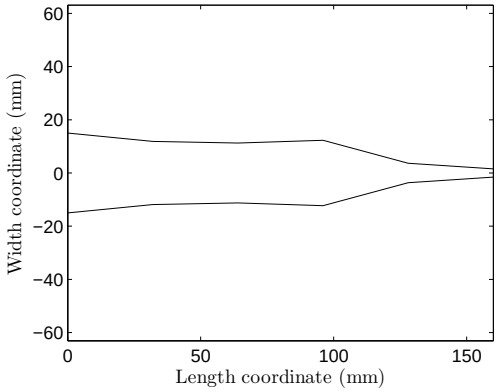

(a) Third suggestion using 5 control points.

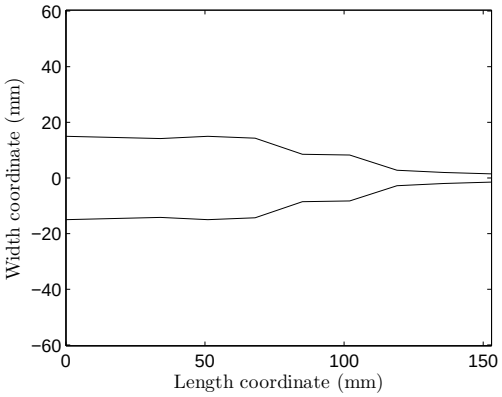

(b) Optimised structure using 10 control points.

Figure 4.4.9: Optimal shape outlines for a 2D structure without holes.

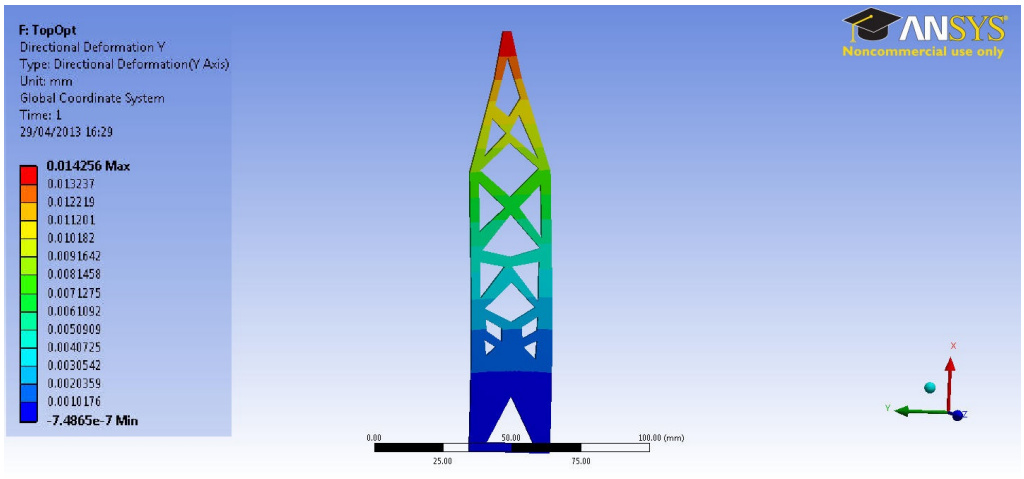

Figure 4.4.10: Interpretation of 2D topology optimisation and its deformation.

Table 4.4.1: ANSYS simulation results. The predicted deformation from the goal-driven optimisation and the simulation results of the actual designs are shown.

t (mm)	Predicted (mm)	Simulated (mm)
Fig. 4.4.8(a)	0.0203	0.0220
Fig. 4.4.8(b)	0.0210	0.0349
Fig. 4.4.9(a)	0.0225	0.0235
Fig. 4.4.9(b)	0.0215	0.0176
Fig. 4.4.10	-	0.0143
Rectangle	-	0.03575
Triangle	-	0.01831

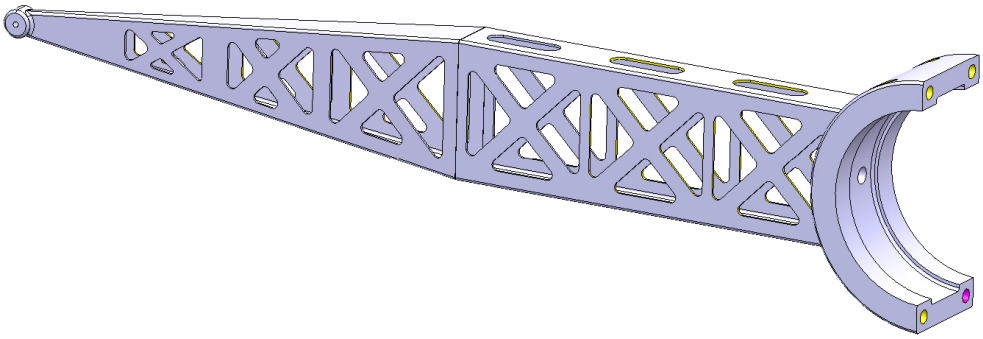

Figure 4.4.11: CAD-model of the final fork.

2D topology optimisation. This is a motivation for using a shape outline corresponding to Fig. 4.4.9(b) but with an internal truss structure.

4.4.6 Final fork design

The findings of the optimisation studies are combined into a final fork design. The shape outline of the fork is selected to use a width of 30 mm for the first half of the fork length. The fork then narrows linearly towards the tip. In the thickness direction (*i.e.*, the direction of the wire) the thickness is also constant for the first half of the fork and then similarly narrows linearly until the tip is reached. The final design has a truss structure and is void of material in the centre to lower the inertia. To further lower the inertia, titanium is chosen as the material. A further reason for this choice is that titanium forks are cheaper to manufacture than stainless steel forks, when metal additive manufacturing is used. The final fork design is shown in Fig. 4.4.11.

The deformation of the fork and the equivalent stresses at maximum acceleration using a square acceleration profile are shown in Fig. 4.4.12. The maximum vibrational amplitude is computed to 40 μm. The equivalent stress in the part is low, the maximum is computed to 7.5 MPa which is far under the yield strength of approximately 950 MPa and the fatigue limit of around 450 MPa for most titanium alloys.

4.4.7 Transient simulation of the fork

The results of the modal analysis are shown in Tab. 4.4.2. The three lowest modes that are displayed correspond to modes that can be excited by the applied acceleration, *i.e.*, those that vibrate in the rotational direction. From the table it can be seen that the lowest eigenfrequency is approximately 1 kHz.

The simulated vibrational behaviour of the proposed fork design is shown in Fig. 4.4.13. It can be seen that the maximum amplitude of the vibrations when the wire passes through the beam pipe is as high as 100 μm with a frequency of approximately 1 kHz, corresponding to the fork's first eigenmode. This is far from the maximum acceptable uncertainties in the measurements of 5 μm. Although no damping is used in the model

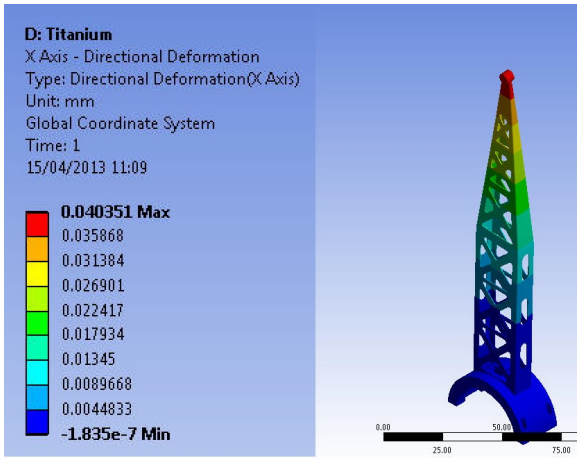

(a) Fork deformation.

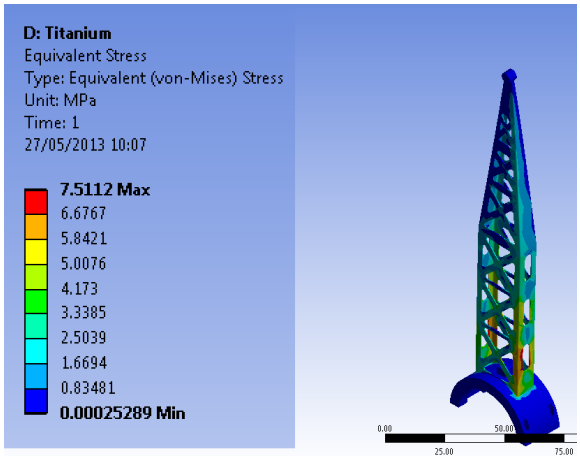

(b) Equivalent stress.

Figure 4.4.12: Deformation and equivalent (von Mises) stress of suggested fork design at maximum acceleration using a square acceleration profile.

Table 4.4.2: Eigenmodes and corresponding frequencies of the fork.

Mode	f (Hz)
1	977
2	3606
3	7103

the vibrations are still tuned out. This phenomenon appears due to the tensile force in the fork that is a consequence of the rotational velocity.

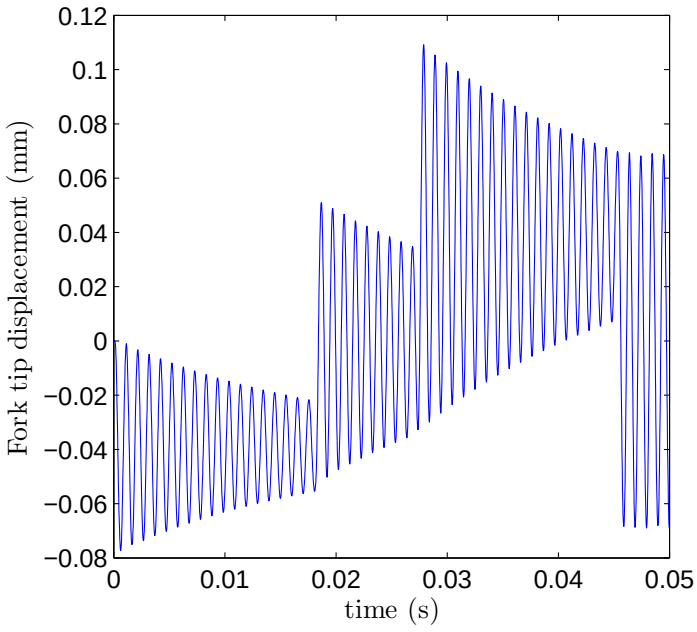

Figure 4.4.13: Deformation of suggested fork design, with a coordinate system following the rotation, with respect to its undeformed state. A square acceleration profile is used.

4.5 Transient simulation of the shaft assembly

The tip deflections of the two forks when the shaft is accelerated are shown in Figs. 4.5.1 and 4.5.2. The results show that the acceleration profile has a large influence on the vibrations of the forks. The square acceleration profile gives rise to violent vibrations already from the start of the scan (see Fig. 4.5.1). Since the vibrations are so large that the two forks' positions with respect to the undeformed configuration cross, an interesting dynamic behaviour is obtained. The vibration of the first fork (the one near the motor) is damped and then increases again due to that the two forks' vibrations are slightly out of phase with each other. This probably occurs due to the dynamics of the shaft.

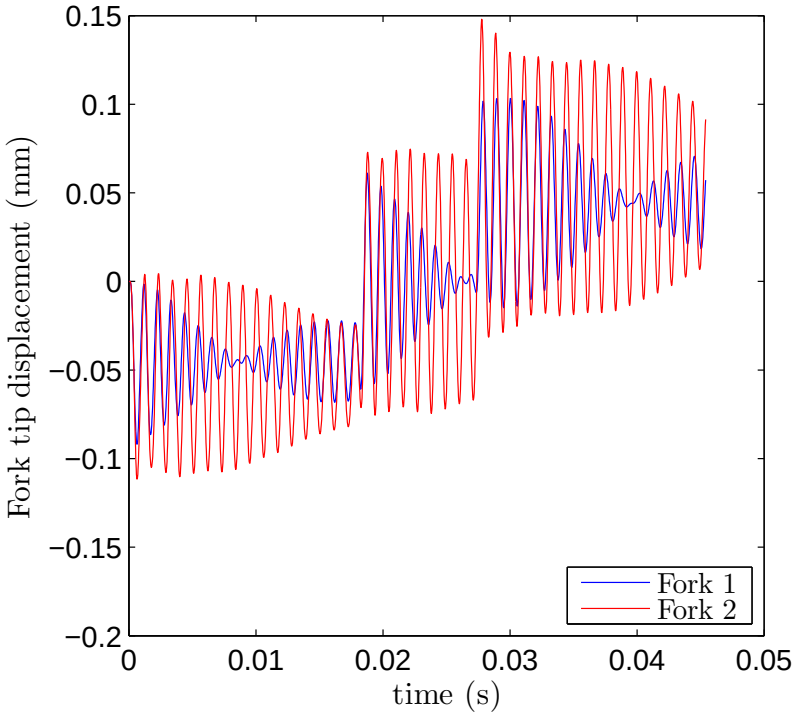

Figure 4.5.1: Fork tip deflections for the two forks as simulated in the shaft assembly. The coordinate system follows the rotation, with respect to its undeformed state. Fork 1 is the fork closest to the motor.

Figure 4.5.2 shows that a smooth start of the acceleration reduces the amplitude of the vibrations significantly. The smoother of the acceleration profiles (case (b)) has the lowest vibrations but also has a higher maximum deflection of the tip due to that a higher peak acceleration must be used to reach the scanning speed of 20 m/s.

The precision requirements on the wire scanner come from the maximum allowed offset in the region of interest defined in Sec. 1.3. With the smooth, sinusoidal acceleration profiles in the uncertainties of the fork tip position are well below the limit of 5 μm, as Fig. 4.5.3 shows. The resulting offset is in the range of 1 μm when the wire passes through the beam. Although the maximum deflection of the fork tips during the scan is higher in case (b) the offset is slightly lower than in case (a) due to that the acceleration is lower when the wire passes through the beam. When analysing these results it should be noted, however, that additional uncertainties in the measurements can come from the behaviour of the wire and optical encoder system, which are not treated in this thesis. Nevertheless, a simulated wire offset of around 1 μm is seen as sufficiently small to create a good opportunity for keeping the total measurement error below 5 μm. This motivates the decision to manufacture the forks according to the suggested fork design.

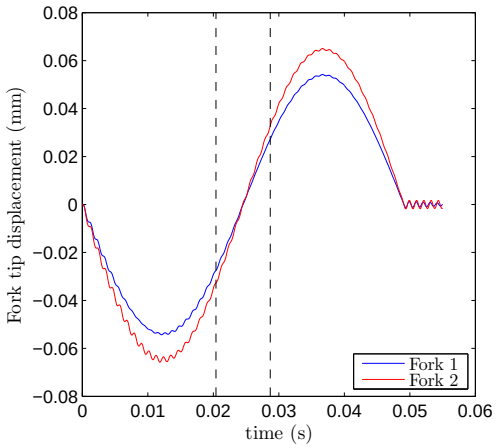

(a) Sinusoidal acceleration.

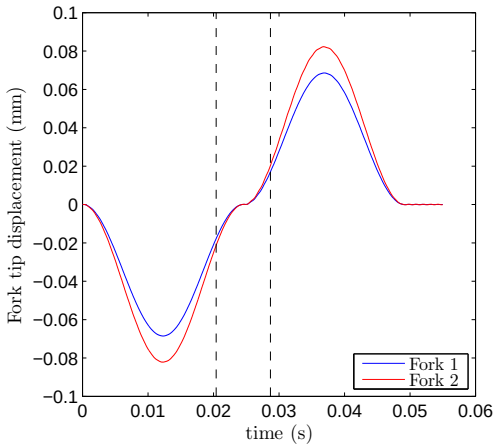

(b) Sinusoidal acceleration with constant wire speed through the beam.

Figure 4.5.2: Deformation of suggested fork design, with a coordinate system following the rotation, with respect to its undeformed state. Fork 1 is the fork closest to the motor. The region between the dashed vertical lines represents the part of the scan which is inside the beam pipe.

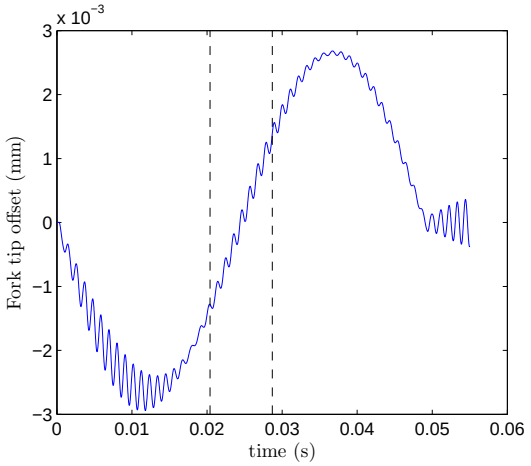

(a) Sinusoidal acceleration.

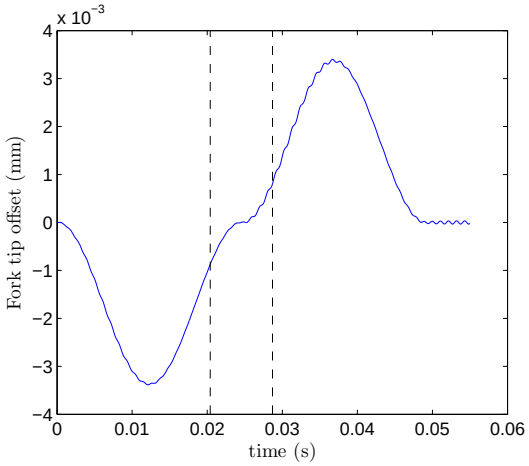

(b) Sinusoidal acceleration with constant wire speed through the beam.

Figure 4.5.3: The offset in the region of interest.The region between the dashed vertical lines represents the part of the scan which is inside the beam pipe.

5 Conclusion

In this master's thesis project, three wire scanner components have been designed and optimised such that they fulfil the requirements imposed on them. A motor housing has been designed, which fits in the air gap of 0.8 mm between the rotor and stator of the electric motor and meets all the structural demands with regard to buckling and radial deformation. Furthermore, a fork and shaft system has been designed and it fulfils the precision requirements of a maximum offset of 5 μm in the region of $\pm$20 mm from the wire centre. The forks have been structurally optimised using topology and shape optimisation methods, which have been shown to be powerful tools in the design process. The method to topologically optimise components subjected to an acceleration load is believed to be a novel approach and has been successfully implemented on a two-dimensional structure in the present thesis. This method has been shown to generate a design which successfully meets the demands on the structure. However, the commercial software used in this thesis, HyperWorks, was not able to generate a feasible design in 3D using acceleration loads, showing that further advances regarding optimisation in three dimensions can be made in the field of topology optimisation. A plastic prototype (see Fig. 5.0.1) of the fork, using a CAD-model which has been developed based on the findings of the optimisation study, has been made at the prototype laboratory at Chalmers University of Technology using 3D-printing, which shows that this is a plausible way of manufacturing the forks. It can be concluded from the present thesis that topology optimisation methods constitute an interesting design tool, especially in conjunction with 3D-printing technology, with a potential for use in the design process for other mechanical components in particle accelerators as well.

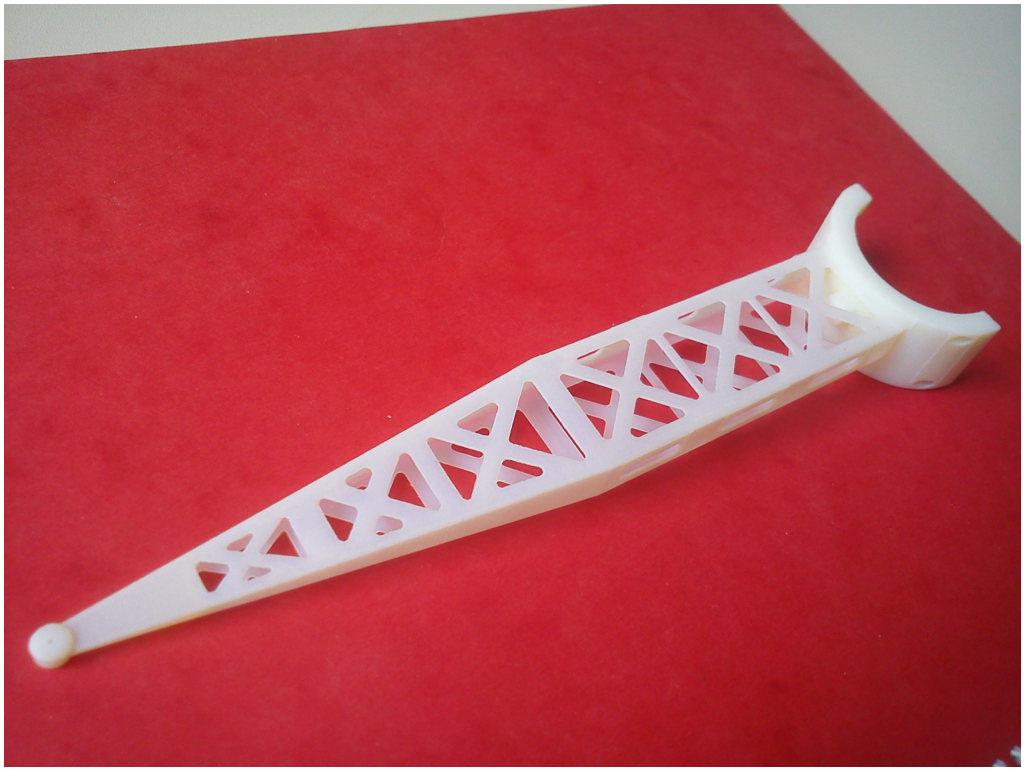

Figure 5.0.1: Plastic prototype of the final fork design.

5.1 Future work

The components that have been designed and optimised in this project have been ordered and will be manufactured during the summer of 2013. The motor housing and shaft will be manufactured on-site by the main workshop at CERN. The titanium forks, on the other hand, will be manufactured externally, according to the CAD-model of the optimised design, using metal additive manufacturing. It remains, however, to qualify the fork for use in a particle accelerator environment, due to that there is little experience using

components manufactured using this technology in ultra-high vacuum conditions. To this end, vacuum tests will be carried out by the vacuum group at CERN. This stated, in the event that 3D-printed forks have a too high outgassing rate, the findings of this thesis can still be used if the fork design is modified for manufacturing using conventional machining methods.

The finished components will be installed in a first prototype of the new fast wire scanner which will be tested in a laboratory during the autumn of 2013. The findings of these experiments will then be used to evaluate if any changes have to made before a second prototype is installed into the SPS during the course of 2014. Related to the work conducted in the present thesis, it will be especially interesting to see how the dynamics of the fork and shaft interact with the wire dynamics. With the experience gained from the prototype installed in the SPS, a final design which can hopefully be integrated into all of the accelerators at CERN can be developed for installation during the second long shutdown (LS2) of the CERN accelerators, due to take place in 2018 and 2019. The author of this master's thesis sincerely hopes that much of the work carried out during the course of this thesis will be of benefit in this process.

References

[1] CERN. *Research at CERN: a gateway to the universe*. Feb. 2013. URL: http://public.web.cern.ch/public/en/Research/Research-en.html.

[2] CERN. *LHC - The Guide*.

[3] ATLAS Collaboration. "A Particle Consistent with the Higgs Boson Observed with the ATLAS Detector at the Large Hadron Collider". In: *Science 338* (2012), pp. 1576–1582.

[4] CMS Collaboration. "A New Boson with a Mass of 125 GeV Observed with the CMS Experiment at the Large Hadron Collider". In: *Science 338* (2012), pp. 1569–1575.

[5] Lyndon R. Evans and Philip Bryant. "LHC Machine". In: *Journal of Instrumentation 3* (2008).

[6] Peter Forck. *Lecture Notes on Beam Instrumentation and Diagnostics*. Lecture notes. Gesellschaft für Schwerionenforschung (GSI), Darmstadt, Germany, 2009.

[7] Bernd Dehning et al. "Vacuum Actuator and Controller Design for a Fast Wire Scanner". In: *Proceedings of BIW2012*. 2012, pp. 195–197.

[8] Mohamed Koujili et al. "Design of an Actuator for the Fast and High Accuracy Wire Scanner". In: *2011 IEEE International Electric Machines & Drives Conference (IEMDC)* (2011), pp. 1450–1455.

[9] Raymond Veness et al. "Design of a High-precision Fast Wire Scanner for the SPS at CERN". In: *Proceedings of IBIC2012*. 2012.

[10] Jose Luis Sirvent Blasco. "Design of an optical fibre based angular position sensor for wire scanners complying with ultra-high vacuum, high temperature and radiation conditions of the CERN´s accelerators". MA thesis. Spain: Miguel Hernandez U., 2012.

[11] Kenneth Runesson and Fredrik Larsson. *Buckling Analysis - Theory and Computation*. Lecture notes. Chalmers University of Technology, Gothenburg, Sweden, 2006.

[12] ANSYS Inc. *ANSYS - Simulation Driven Product Development*. Feb. 2013. URL: http://www.ansys.com/.

[13] ANSYS Inc. *ANSYS Mechanical APDL Theory Reference*.

[14] Gerald Kress and David Keller. *Structural Optimization*. Lecture notes. Zentrum für Strukturtechnologien, ETH Zurich, Switzerland, 2007.

[15] Erik Andreassen et al. "Efficient Topology Optimization in MATLAB Using 88 Lines of Code". In: *Struct Multidisc Optim 43* (2011), pp. 1–16.

[16] P. Pedersen. *Optimal Designs*. Tech. rep. Department of Mechanical Engineering, Solid Mechanics, Technical University of Denmark, Lyngby, Denmark, 2003.

[17] Sheldon Imaoka. *Analyzing Buckling in ANSYS Workbench Simulation*.

[18] Kim J.R. Rasmussen. *Full-range Stress-strain Curves for Stainless Steel Alloys*. Tech. rep. Department of Civil Engineering, Centre of Advanced Structural Engineering, University of Sydney, Australia, 2001.

[19] Michael F. Ashby. *Materials Selection in Mechanical Design*. Butterworth-Heinemann Ltd.

[20] ANSYS Inc. *Design Exploration User Guide*.

[21] D. Coyne. *LIGO Vacuum Compatible List*. Tech. rep. LIGO Science Collaboration, 2004.

[22] Stefano Sgobba. "Materials of High Vacuum Technology, An Overview". In: *CAS - CERN Accelerator School and ALBA Synchrotron Light Facility: Course on Vacuum in Accelerators*. 2006, pp. 117–144.

[23] Wikipedia. *Beryllium - Wikipedia, the free encyclopedia*. Feb. 2013. URL: http://en.wikipedia.org/wiki/Beryllium.

[24] Wikipedia. *Molybdenum - Wikipedia, the free encyclopedia*. Feb. 2013. URL: http://en.wikipedia.org/wiki/Molybdenum.

[25] Warren C. Young. *Roark's Formulas for Stress and Strain*. McGraw-Hill Inc.

[26] Mart Mägi and Kjell Melkersson. *Lärobok i maskinelement*. EcoDev International AB.